remote sensing

MDPI

Article

Atmospheric Anomaly Analysis Related to Ms > 6.0 Earthquakes in China during 2020–2021

Xitong Xu, Shengbo Chen *, Yan Yu and Sen Zhang

College of Geo-Exploration Science and Technology, Jilin University, Changchun 130026, China; xitong19@mails.jlu.edu.cn (X.X.); yuyan14@mails.jlu.edu.cn (Y.Y.); zhangsen19@mails.jlu.edu.cn (S.Z.)
* Correspondence: chensb@jlu.edu.cn

Abstract: The attention towards links of atmospheric parameter variation and earthquakes has increased exponentially by utilizing new methods and more accurate observations. Persistent research makes it possible to gain insight into the precursor mechanism of earthquakes. In this paper, we studied the universality of detecting atmospheric anomalies associated with earthquakes based on tidal force fluctuation in China for earthquakes of Ms > 6.0, and explored the influence of tidal force on tectonic stress. The data of air temperature, geopotential height, ozone mixing ratio, and relative humidity from the National Center for Environmental Prediction (NCEP) were analyzed to reveal the spatiotemporal variation of atmospheric anomalies at multiple isobaric surfaces. Furthermore, the coupling of atmospheric parameters was investigated. The results showed that continuous solicitation exerted by tidal forces could change the strength of tectonic stress that causes earthquakes. The evolution pattern of air temperature, geopotential height, and relative humidity could be supported by atmospheric thermal vertical diffusion, while the anomalies of ozone mixing ratio was not evident. This verified the feasibility of detecting multi-parameter atmospheric anomalies associated with earthquakes based on tidal force fluctuation. Our results provide more evidence for understanding the atmospheric precursor characteristics of earthquakes.

Keywords: earthquake; tidal force; atmospheric anomaly; multiple isobaric surface; Ms > 6.0

check for updates

Citation: Xu, X.; Chen, S.; Yu, Y.; Zhang, S. Atmospheric Anomaly Analysis Related to Ms > 6.0 Earthquakes in China during 2020–2021. *Remote Sens.* **2021**, *13*, 4052. https://doi.org/10.3390/rs13204052

Academic Editor: Carmine Serio

Received: 8 September 2021
Accepted: 7 October 2021
Published: 11 October 2021

Publisher's Note: MDPI stays neutral with regard to jurisdictional claims in published maps and institutional affiliations.

Copyright: © 2021 by the authors. Licensee MDPI, Basel, Switzerland. This article is an open access article distributed under the terms and conditions of the Creative Commons Attribution (CC BY) license (https://creativecommons.org/licenses/by/4.0/).

1. Introduction

There are numerous anomaly reports associated with earthquakes, not only on earth surface but multiple disturbances are also reported in atmosphere during seismic preparation period [1–10]. In particular, thermal anomaly has been widely studied as the impending earthquake anomaly because of its correlation with tectonic activity and high temporal resolution of thermal infrared satellite data [11]. Various theoretical reports were conducted to propose the methods for identifying thermal anomalies related to earthquakes. In the early research of seismic thermal anomaly detection, different methods for interpreting large areas were applied to infrared and land surface temperature measurements [2,3,12,13]. The Robust Satellite Technique (RST) data analysis approach was developed based on the multi-temporal analysis of a historical dataset to detect seismic thermal anomalies [14,15]. Wavelet transform was also applied to extract seismic thermal anomalies by researchers [16,17]. However, the above methods depend on historical data of a long time series, thereby the measurement of small thermal variation related to earthquake is considered unreliably [18]. Furthermore, the images acquired by thermal infrared sensors onboard satellites are affected by high cloud cover [19–21]. Although detection of thermal anomalies is often disrupted by historical data and cloud, these obstacles can be avoided through proper methodology and background data. The tidal forces induced by celestial bodies can cause tectonic stress in the rocks to achieve critical state that triggers earthquakes [22]. The changes in tidal forces and thermal anomaly phenomenon related to seismic activity reflect the mutation of tectonic activities [18,23]. A related research shows that tidal forces, as the method of pre-calculating Earth deformation phenomena, serves

as a certain indicative function for earthquakes in the time domain [24]. In order to avoid the interference of historical data and cloud, the tidal force fluctuant analysis (TFFA) and multiple layers of air temperature have been combined to detect seismic thermal anomalies and reveal warming phenomenon before the earthquake [25,26]. Nevertheless, the method has only been applied in certain earthquakes, and its universality remains to be verified.

In addition to thermal anomalies, the abnormal signals of various atmospheric parameters associated with earthquakes were also observed around the world [27–31]. The observation of atmospheric parameter variation has been combined with other spheres (e.g., lithosphere and ionosphere) to explore the coupling relationship between different spheres associated with earthquakes by researchers [32–34], while the coupling phenomenon between various atmosphere parameter is also significant for understanding precursor mechanism of earthquakes. At present, the research of atmospheric anomalies associated with earthquakes focuses on the variation on time scale and two-dimensional spatial distribution, and abnormal variation of multi-parameters have been observed [9,16,29,31]. However, systematic observation of the vertical evolution in atmospheric anomalies associated with earthquakes is still scarce. Therefore, exploring the spatiotemporal variation of atmospheric anomalies at multiple isobaric surfaces and the coupling of atmospheric parameters can help us to better understand the precursor mechanism of earthquakes.

In the paper, we study the integrated approach of tidal force fluctuation and multiple-layer atmospheric parameters to explore the disturbances in atmosphere that can be linked to earthquakes (Ms > 6.0) in China during 2020–2021. The main objective of this paper is to evaluate the influence of tidal force fluctuation on tectonic stress and investigate the morphological characteristics of atmospheric anomalies associated with earthquakes. Furthermore, we discuss in detail the coupling of air temperature, geopotential height, ozone mixing ratio, and relative humidity.

2. Data and Methods

2.1. Tectonic Environment of Earthquakes

In the study, a total of six earthquakes (Ms > 6.0) in China during 2020–2021 are investigated with atmospheric measurements during 5 periods of tidal force potential. The information of the earthquakes is obtained from the China Seismographic Network and United States Geological Survey. At first, the method proposed by Genzano et al. [35] was used for earthquake declustering. The geographical location of epicenters is shown in Figure 1. Meanwhile, the detailed information of earthquakes is listed in Table 1.

2.2. Meteorological Data

The atmospheric measurement data are provided by the National Center for Environmental Prediction (NCEP)as a product of atmospheric data conducted by NCEP and the National Center for Atmospheric Research (NCAR) since 1991 [36]. The NCEP data are developed after assimilating meteorological observations from the global satellite observation data, global ground observation data, ocean data, radiosonde data, and unmanned aerial vehicle data, etc. The NCEP data, available at 28 pressure levels with $1^\circ \times 1^\circ$ horizontal spatial resolution and 6-hour temporal resolution, offer the most comprehensive, global reanalysis of meteorological data [37].

In this study, spatial and temporal anomalies of air temperature, geopotential height, ozone mixing ratio, and relative humidity are investigated over the earthquake preparation zone to explore atmospheric anomalies induced by earthquake. In order to further investigate variability in the atmosphere caused by earthquakes, multiple layers of atmospheric parameters are selected. Due to the various altitude of different epicenters, five isobaric surfaces with the shortest distance above the epicenter were selected for each earthquake, as shown in Table 2.

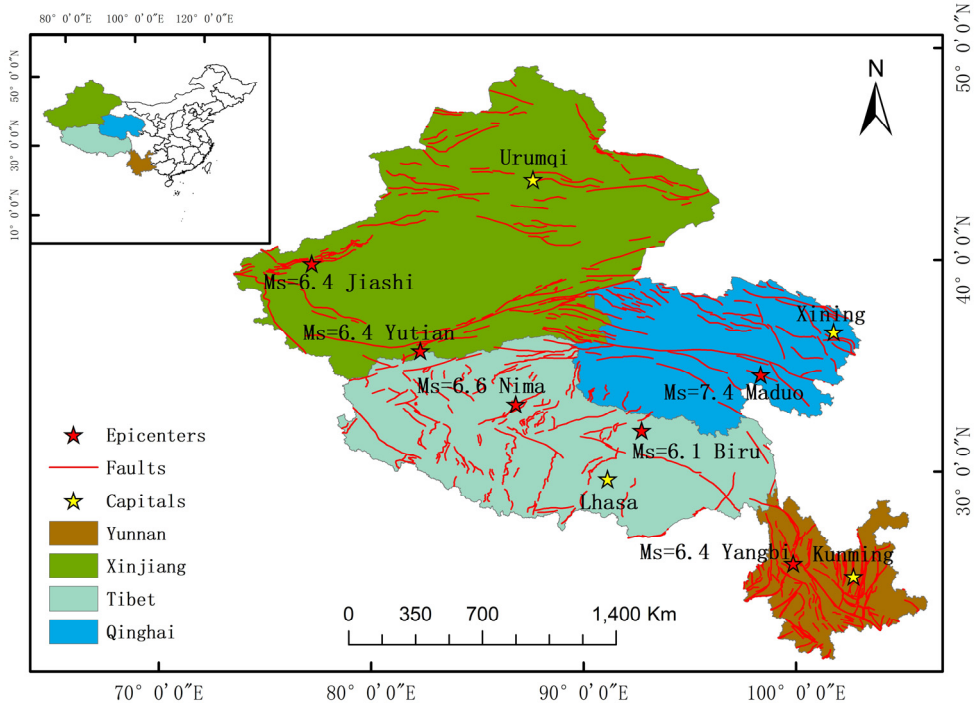


Figure 1. Geographical location of the six earthquakes (Ms > 6.0) in China during 2020–2021. The red stars, red lines, and yellow stars represent the epicenters, faults, and capitals, respectively.

Table 1. Essential characteristics of the studied earthquakes.

Site	UTC Time	Epicenter Location (°)	Ms	Depth (km)	Altitude (m)	Epicenter Fault
Maduo county, Qinghai	18:04, 21 May 2021	N34.59–E98.34	7.4	10	4236	Maduo-Gande
Yangbi county, Yunnan	13:48, 21 May 2021	N25.67–E99.87	6.4	9	2291	Weixi-Qiaohou
Biru county, Tibet	06:11, 19 March 2021	N31.94–E92.74	6.1	8	4474	Southern Margin of Ando Basin
Nima county, Tibet	20:07, 22 July 2020	N33.19–E86.81	6.6	10	5378	Yibug Caka-Rigain Pünco
Yutian county, Xinjiang	21:05, 25 June 2020	N35.73–E82.33	6.4	10	5279	Altun Tagh
Jiashi county, Xinjiang	13:27, 19 January 2020	N39.83–E77.21	6.4	5.6	1399	Kalpintag

Table 2. The selection of isobaric surfaces and data time for the studied earthquakes.

Earthquake	Isobaric Surfaces	Data Time
Maduo	550 hPa, 500 hPa, 450 hPa, 400 hPa, 350 hPa	UTC-18:00
Yangbi	750 hPa, 700 hPa, 650 hPa, 600 hPa, 550 hPa	UTC-12:00
Biru	550 hPa, 500 hPa, 450 hPa, 400 hPa, 350 hPa	UTC-06:00
Nima	500 hPa, 450 hPa, 400 hPa, 350 hPa, 300 hPa	UTC-18:00
Yutian	500 hPa, 450 hPa, 400 hPa, 350 hPa, 300 hPa	UTC-0:00 (next day)
Jiashi	850 hpa, 800 hPa, 750 hPa, 700 hPa, 650 hPa	UTC-12:00

2.3. Tidal Force and the TFFA Method

The tidal force induced by the sun and the moon have macroscopic effects on the earth, and it is one of the important external causes of ground stress [38]. Tidal force causes periodic stress changes in the earth's interior. The accuracy description of calculating the tidal force potential can be found in [23,39]. In the study, the tidal force potential of epicenters was considered at a time scale of 24 h, and the calculation time of daily tidal force potential was consistent with earthquake occurrence time, as shown in Table 1.

The TFFA method proposed by Ma et al. [39] was applied to extract thermal anomalies related to earthquakes, and it was described in detail by Zhang et al [25]. TFFA first divides the data into different periods according to the variation of daily tidal force potential. The first day of each period is set as the background, and thermal anomalies associated with

earthquakes are identified by comparing other data with the background. However, the method can be further modified in terms of period division. In the modified method, the top or trough adjacent to the day of earthquake is considered as the first day of each period. Genzano et al. analyzed thermal anomalies of earthquakes in Japan for 11 consecutive years. They found that few thermal anomalies occurred near the day of earthquakes occurrence, and most earthquakes were apart from thermal anomalies at least a week [35]. Therefore, the trough or top near earthquake is more suitable as the background. The modified period division of TFFA is described as:

- If the earthquake occurred at the top of tidal force, then each top is taken as the first day of each period. Similarly, if the earthquake occurred at the trough, then each trough is taken as the first day of each period.
- If the earthquake did not occur at the trough or the top, time distance is used as the standard. We choose the one closer to the time of earthquake. If the trough and top are equidistant from the time of earthquake, the preceding trough or top is taken as the first day of each period.

After period division, the variations of atmospheric parameters can be calculated based on the background. ΔT, ΔG, ΔH, and ΔO are defined as Equation (1), and the first day of each period is considered as background.

$$\begin{cases} \Delta T = T_d - T_{background} \\ \Delta G = G_d - G_{background} \\ \Delta H = H_d - H_{background} \\ \Delta O = O_d - O_{background} \end{cases} \quad (1)$$

where T_d is the temperature of a day except background, $T_{background}$ is the temperature of the background, G_d is the geopotential height of a day except background, $G_{background}$ is the geopotential height of the background, H_d is the relative humidity of a day except background, $H_{background}$ is the relative humidity of the background, O_d is the ozone mixing ratio of a day except background, and $O_{background}$ is the ozone mixing ratio of the background.

2.4. Specific Criteria for Selecting Atmospheric Thermal Anomalies Related to Earthquakes

Atmospheric temperature is affected by many factors, and it has many forms of evolution. In particular, Ma et al. [26] indicated that the process of atmospheric thermal anomalies related to earthquakes is similar to thermal infrared (TIR) variation of rocks that broke under stress loading. The identification of atmospheric thermal anomalies requires the definition of a threshold. The evolution of atmospheric thermal anomalies is a continuous process, in fact, thermal anomalies appear at the bottom and dissipate in the upper layer. Atmospheric thermal anomalies have a steep change in temperature from high to low on the spatio-temporal scale [26]. High threshold could make the evolution pattern ignored. The problem can be avoided by obtaining a set of atmospheric thermal anomalies with a lower threshold and then identifying the thermal anomalies associated with earthquakes according to the evolution pattern. Therefore, the threshold φ is set as Equation (2).

$$\varphi = \overline{\Delta T} + \sigma_{\Delta T} \quad (2)$$

where $\overline{\Delta T}$ is the mean of ΔT for the entire study area within the total study duration, and $\sigma_{\Delta T}$ is the standard deviation of ΔT for the entire study area within the total study duration.

In order to identify atmospheric thermal anomalies related to earthquakes, we established the specific criteria including spatial distribution, temporal persistence, and relative intensity:

- The threshold φ is used to detect thermal anomalies;
- Thermal anomalies appear at the bottom and lift towards the top. As height increases, the thermal anomalies diminish;

- The distribution of thermal anomaly at each vertical level coincide with the fault pattern;
- Thermal anomalies should be extended on time scale, so that thermal anomalies should last two consecutive days at least.

Atmospheric thermal anomalies of each earthquake were identified according to above criteria, and then ΔG, ΔH, and ΔO of corresponding days were also listed to analyze atmospheric evolution.

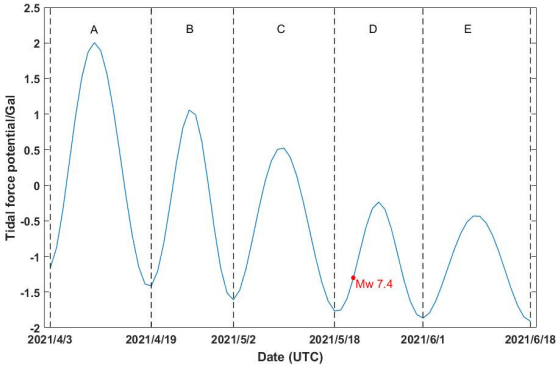
3. Results

3.1. Change in Tidal Force and Determination of Period

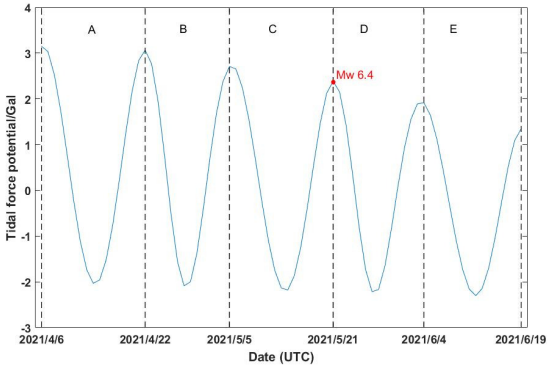
The tidal force potential of epicenters was calculated at a time scale of 24 h, and the calculation of tidal force potential was performed at earthquake occurrence time every day. The daily tidal force potential at the hypocenter of studied earthquakes was calculated, as shown in Figure 2. For each earthquake, the time series was divided into five periods, and each period was labeled as A, B, C, D, and E, respectively. The Ms 7.5 earthquake in Maduo and the Ms 6.1 earthquake in Biru occurred at the inflection points of period D, and other earthquakes occurred around the day when the tidal force potential was at peak. In addition, the specific dates of each period for earthquakes are listed in Table 3.

3.2. Atmosphere Evolution during Atmospheric Thermal Anomalies

The specific criteria for selecting atmospheric thermal anomalies related to earthquakes was applied to all periods of each earthquake, and atmospheric thermal anomalies were identified in four earthquakes, as shown in Table 4. In earthquakes of Maduo and Yutian, no atmospheric thermal anomaly was detected. In Yangbi, the last day of atmospheric thermal anomaly occurred 30 days before the earthquake. In Biru, the last day of atmospheric thermal anomaly occurred 19 days before the earthquake. In Nima, the last day of atmospheric thermal anomaly occurred 33 days before the earthquake. In Jiashi, the last day of atmospheric thermal anomaly occurred 21 days before the earthquake.



(**a**)



(**b**)

Figure 2. *Cont.*

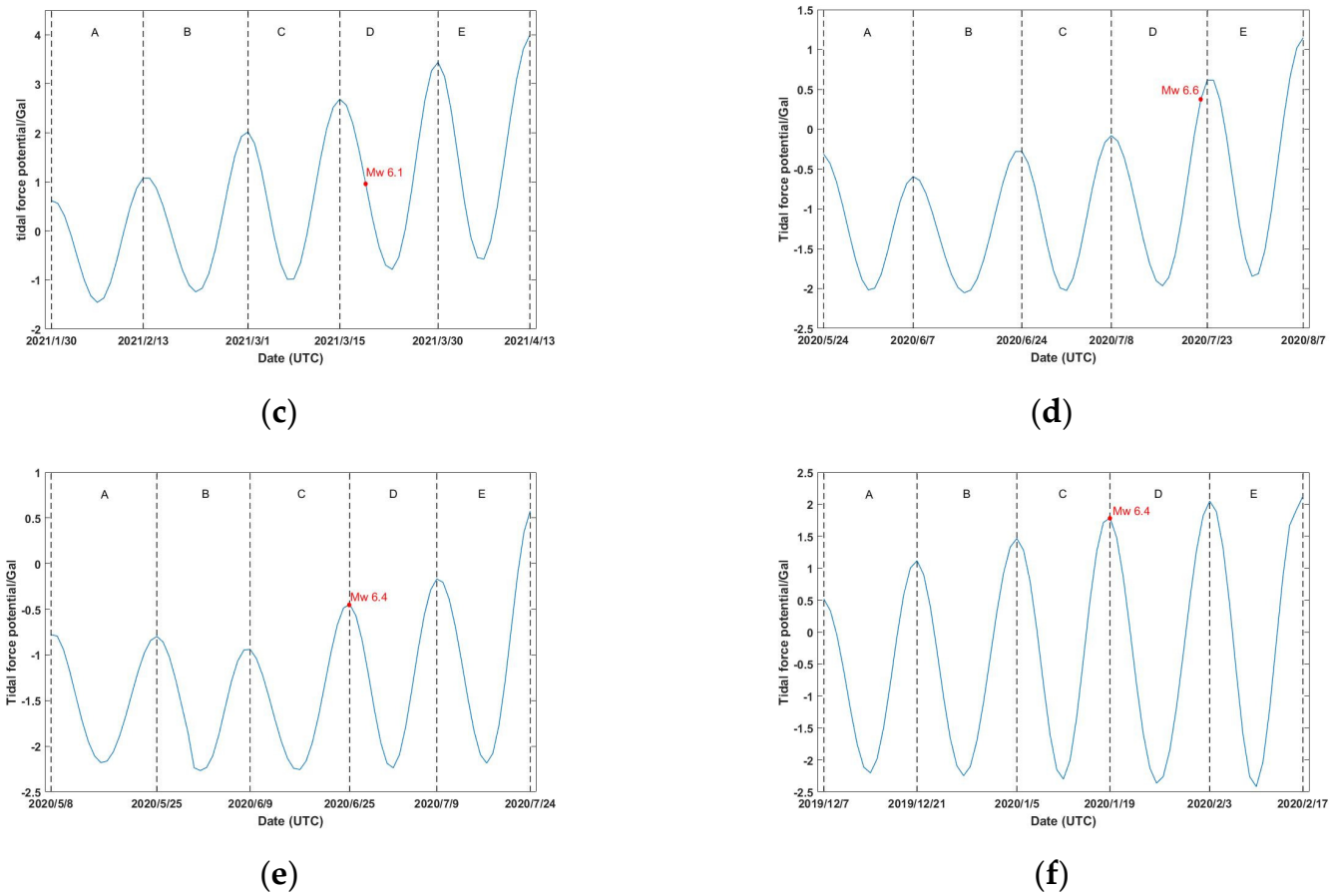


Figure 2. The change in tidal force potential for earthquake in (**a**) Maduo, (**b**) Yangbi, (**c**) Biru, (**d**) Nima, (**e**) Yutian, (**f**) Jiashi. The red points are the dates of earthquakes.

Table 3. The date range of each period for the studied earthquakes.

Earthquake	Period A	Period B	Period C	Period D	Period E
Maduo	3 April−18 April	19 April−1 May	2 May−17 May	18 May−31 May	1 June−17 June
Yangbi	6 April−21 April	22 April−4 May	5 May−20 May	21 May−3 June	4 June−18 June
Biru	30 January−12 February	13 February−28 February	1 March−14 March	15 March−29 March	30 March−12 April
Nima	24 May−6 June	7 June−23 June	24 June−7 July	8 July−22 July	23 July−6 August
Yutian	8 May−24 May	25 May−8 June	9 June−24 June	25 June−8 July	9 July−23 July
Jiashi	7 December−20 December	21 December−4 January	5 January−18 January	19 January−2 February	3 February−16 February

Table 4. The periods and specific date of atmospheric thermal anomalies.

Earthquake	Period of Atmospheric Thermal Anomalies	Specific Date
Maduo	-	-
Yangbi	A	7 April−21 April
Biru	B	21 February−28 February
Nima	B	8 June−19 June
Yutian	-	-
Jiashi	B	25 December−29 December

In order to provide more evidence to atmospheric anomalies, other processes within the atmosphere over each earthquake were monitored by spatial and temporal analysis of geopotential height, ozone mixing ratio and relative humidity during atmospheric thermal anomalies. The most obvious thermal anomalies and corresponding atmospheric parameters are shown in Figures 3–6, and the composite atmospheric evolution was pre-

sented in Figures A1–A4 (dynamic evolution of atmospheric parameters is in Appendix A). Figures 3–6 correspond to earthquakes in Yangbi, Biru, Nima, and Jiashi, respectively.

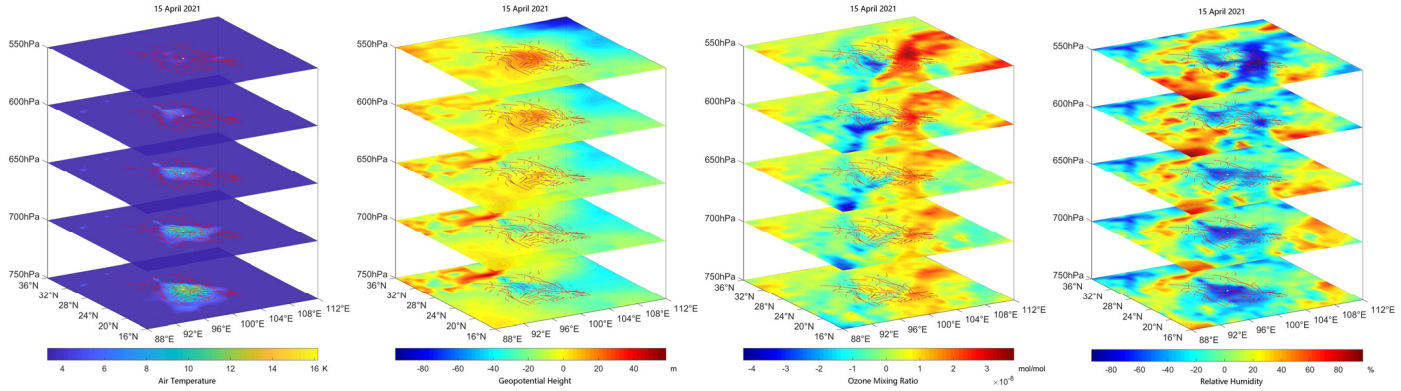


Figure 3. Composite atmospheric anomaly map associated with earthquake in Yangbi on 15 April. The epicenter and faults are shown by yellow point and red lines, respectively. For each row, the subplots represent air temperature, geopotential height, ozone mixing ratio and relative humidity from left to right.

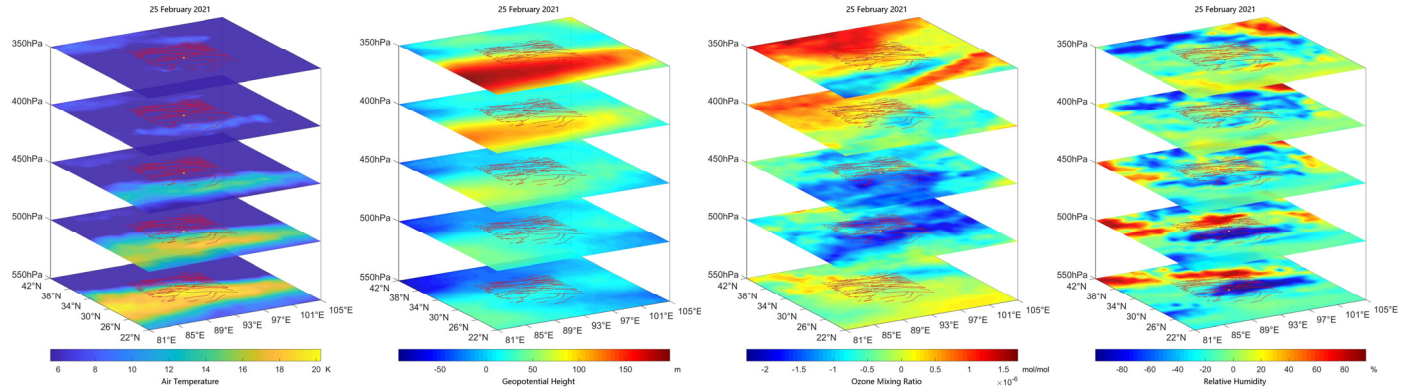


Figure 4. Composite atmospheric anomaly map associated with earthquake in Biru on 25 February. The epicenter and faults are shown by yellow point and red lines, respectively. For each row, the subplots represent air temperature, geopotential height, ozone mixing ratio and relative humidity from left to right.

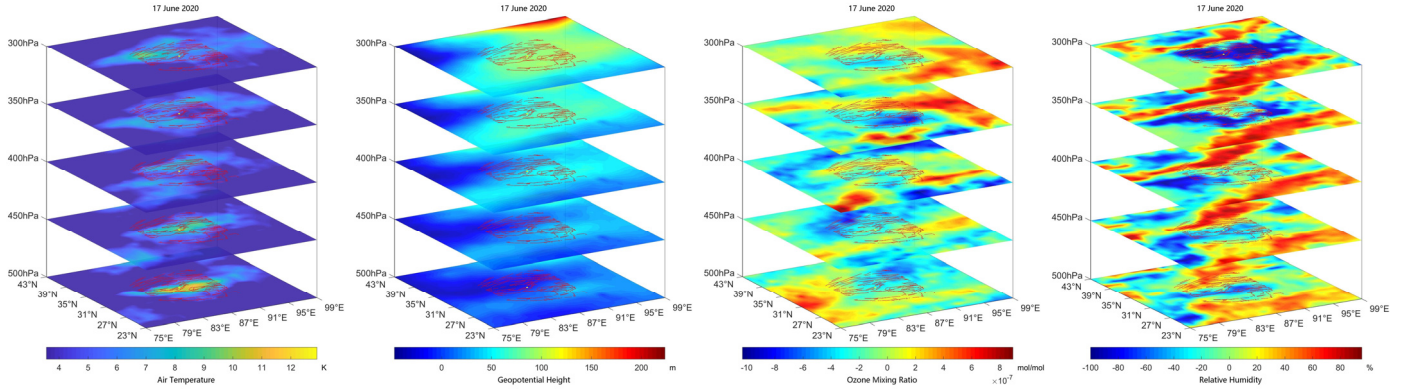


Figure 5. Composite atmospheric anomaly map associated with earthquake in Nima on 17 June. The epicenter and faults are shown by yellow point and red lines, respectively. For each row, the subplots represent air temperature, geopotential height, ozone mixing ratio and relative humidity from left to right.

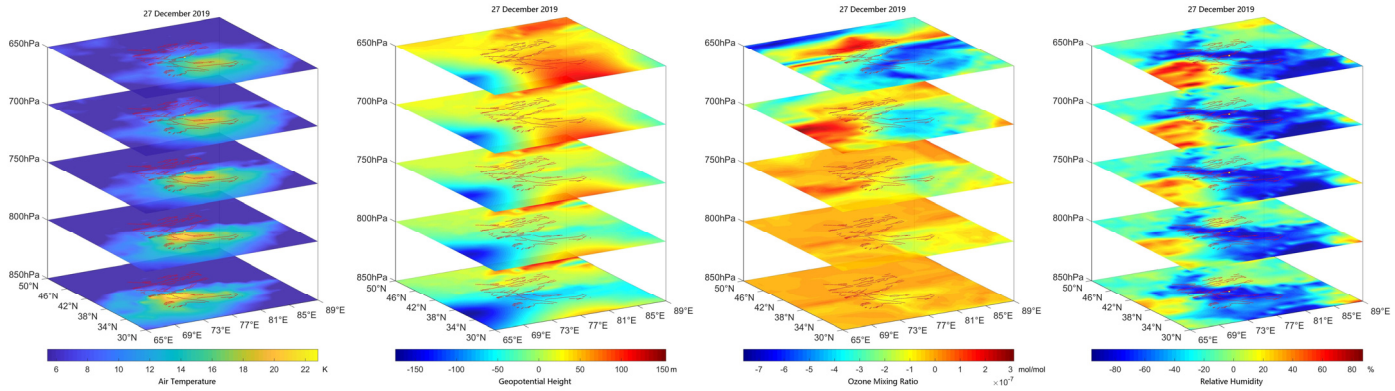


Figure 6. Composite atmospheric anomaly map associated with earthquake in Jiashi on 27 December. The epicenter and faults are shown by yellow point and red lines, respectively. For each row, the subplots represent air temperature, geopotential height, ozone mixing ratio and relative humidity from left to right.

During atmospheric thermal anomalies, their distribution was consistent with fault pattern for each earthquake. The atmospheric thermal anomalies in Yangbi lasted throughout period A. It is obvious that thermal anomalies appeared at the bottom and lift towards the top with a fading trend. For geopotential height, the trend was not evident on 7 April. Since 8 April, the geopotential height on the top isobaric surface had been abnormal in the position similar to thermal anomalies. The trend of geopotential height anomalies was opposite to that of thermal anomalies, which gradually disappears from the top to the bottom. This phenomenon could be observed throughout the duration of thermal anomalies. In the period, the variation of ozone mixing ratio had no observable anomalies. In contrast, the negative anomalies of relative humidity over the epicenter were consistent with the thermal anomalies on time scale and spatial distribution. Similar geopotential height and relative humidity anomalies were also evident during thermal anomalies in Biru, and the variance of ozone mixing ratio showed no correlation with the earthquake. In Biru, the opposite trend of geopotential height compared with thermal anomalies was also evident, and geopotential height anomalies peaked on 26 February, one day after the peak of thermal anomalies. In addition, the trend of geopotential height in Nima and Jiashi accorded with that in Yangbi and Biru, while the trend of relative humidity in only Jiashi accorded with that in Yangbi and Biru. The relative humidity anomalies in Nima was not evident in upper layers, and the relative humidity anomalies had a weak similarity with thermal anomalies in spatial distribution. The ozone mixing ratio anomaly was also not observed in Nima and Jiashi.

In summary, the distribution of geopotential height and relative humidity was observed to be similar to that one of thermal anomalies, but the distribution of ozone mixing ratio did not show consistency with that one of thermal anomalies. The positive anomalies of geopotential height had an obvious opposite trend to thermal anomalies, and the trend of negative relative humidity anomalies was consistent with that one of thermal anomalies. In addition, a delay of geopotential height anomalies relative to thermal anomalies was observed.

4. Discussion

Earthquakes occur due to the mechanical process that begins with tectonic stress by subjecting the rocks inside the earth to accumulating energy, culminating in a destructive rupture. Tidal forces act as an external factor, which supplements tectonic stress, exerting an obvious inducing effect on the active fault whose ground stress was at the critical state [23]. Among the studied earthquakes, four of them occurred around peaks of tidal forces, and two of them occurred at the inflection points of tidal forces. This reflects that although tidal forces have an inducing effect on earthquakes, they cannot trigger earthquake directly. The distribution of atmospheric thermal anomalies in Yangbi, Biru, Nima, and Jiashi

obeyed the rule of thermal radiation of rock broken under the stress loading, indicating that atmospheric thermal anomalies are possibly produced by the preparation phase of earthquakes. The atmospheric thermal anomalies of earthquakes in Yangbi and Nima occurred on the first day after the peaks of tidal forces, while the atmospheric thermal anomalies of earthquakes in Biru and Jiashi occurred near the troughs of tidal forces. The continuous solicitation of tidal forces and accumulation of tectonic stress could lead to rock micro-fracture and earthquakes [26]. Therefore, rock micro-fracture and earthquakes are more likely to occur around peaks of tidal forces, but not always.

In addition, the variation of other atmospheric parameters (i.e., geopotential height, ozone mixing ratio, and relative humidity) were observed at isobaric surfaces during atmospheric thermal anomalies. It can be seen that all atmospheric thermal anomalies related to earthquakes were accompanied by consistent geopotential height variation, that is, the positive anomalies of geopotential height appeared at the highest isobaric surface and decayed downward. Heating of the lower isobaric surface is favorable for air mass raising, which can lead to the increasing of geopotential height at upper isobaric surface [40,41]. The atmospheric thermal vertical diffusion associated with the earthquakes involves air being warmed by land, uplifted by heat flux, cooled and dissipated in the sky [26]. The geopotential height variation pattern observed during atmospheric thermal anomalies accords with atmospheric thermal vertical diffusion and air mass migration. In contrast, the relationship between ozone mixing ratio and thermal anomalies was not observed. The content of tropospheric ozone is much lower compared with that of stratospheric ozone, which makes it difficult to distinguish the abnormal variation of tropospheric ozone. The occurrence of tropospheric ozone variance depends on many environmental factors (e.g. dust storms [42], volcanic eruptions [43], etc.), thereby the previous monitoring of tropospheric ozone is based on comparative analysis of long time-series data [44–46]. In particular, the research by Piscini et al. shows that the total column ozone was less statistically significant through analyzing long time-series data [44], and our study indicates that the anomalies of tropospheric ozone in short time-series are also not evident. Therefore, tropospheric ozone may be not an effective parameter that precedes the earthquake occurrence. The negative anomalies of relative humidity observed in Yangbi, Biru, and Jiashi were consistent with thermal anomalies on time scale and spatial distribution, whereas the negative anomalies of relative humidity observed in Nima were observed on the similar time scale as thermal anomalies. Heating of land promoted air movement, air mixing, and an increase in air temperature. This causes the ions to attract water vapor molecules, leading to a decrease in the content of free available water vapor [4,47]. As a result of the phenomenon, negative anomalies of relative humidity are generated.

It should be noted that atmospheric parameters are influenced by many external factors. Strong meteorological phenomena, geological activities, and disasters can lead to significant variation of atmospheric parameters [42,43,48,49]. The air temperature at the top isobaric surface in Nima rises again in part of the time. Such short-term changes may be related to some meteorological activities, and the weak anomalies of relative humidity in Nima may also be caused by this. Furthermore, the absence of observed thermal anomalies in Maduo and Yutian may be also associated with meteorological activities. During the observation of Maduo (3 April−17 June), the weather is undergoing seasonal variation. Due to latitude and altitude, seasonal weather changes greatly increased air temperature in Maduo. In June 2020, a severe heat wave was reported in Yutian. Therefore, the obvious seasonal climate change and short-term intense climate change could affect the detection of atmospheric thermal anomalies. Furthermore, the earthquakes in the study were all shallow (depth $\leq$ 10 km). The anomalies associated with the earthquakes are supposed to be influenced by depth [13]; therefore, further studies are necessary to reveal the influences that depth of earthquakes changes on TFFA.

Among the six studied earthquakes, the atmospheric thermal anomalies were observed at four locations. This suggest that it is feasible to identify atmospheric thermal

anomalies based on tidal force fluctuation. Furthermore, the coupling relationship of thermal anomalies, geopotential height and relative humidity was also observed, indicating that TFFA can be further applied to the identification of atmospheric anomalies associated with earthquakes. However, the detection of atmospheric anomalies is affected by many environmental factors, and the anomalies may be completely covered. The determination of periods in TFFA is also limited by the need to know when an earthquake occurred. This limits the use of the method in forwarding direction to identify earthquake precursors, but the method is significant in the post-analysis of earthquake precursors.

5. Conclusions

In this paper, earthquake-induced atmospheric anomalies have been detected from air temperature, geopotential height, ozone mixing ratio, and relative humidity for six earthquakes based on tidal force fluctuation. Research has shown that it is feasible to identify atmospheric thermal anomalies using TFFA, which is not only suitable for specific earthquakes. Tidal forces can induce rock micro-fracture and earthquakes, but they cannot trigger rock micro-fracture and earthquakes directly. The continuous solicitation exerted by tidal forces can reduce the strength of tectonic stress that causes earthquakes. Correspondingly, the atmospheric thermal anomalies detected in four seismogenic zones only occurred in one of five periods. This implies that tidal forces cause atmosphere temperature changes by altering stress state rather than directly triggering thermal anomalies. Further analysis has demonstrated the coupling relationship of thermal anomalies, geopotential height, and relative humidity, and no anomaly of tropospheric ozone was observed in this study. Atmospheric thermal anomalies obeyed the rule of thermal radiation of rock broken under the stress loading at several locations, providing more evidence for the tectonic stress accumulation and loss in the seismogenic zone. In addition, the positive anomaly variation pattern of geopotential height and the negative anomaly variation pattern of relative humidity could be supported by atmospheric thermal vertical diffusion, and tropospheric ozone may be not an effective parameter that precedes the earthquake occurrence. Coupling phenomena of atmospheric parameters were detected in several seismogenic zones, which could help to identify earthquake atmospheric anomalies, also showing that atmospheric measurement may play an important role for the analysis and prediction of earthquakes. Further studies are recommended to reveal the atmospheric anomalies related to earthquakes with multiple atmospheric parameters and remote sensing data.

Author Contributions: All of the authors contributed to the study. Conceptualization, X.X.; Data curation, X.X., Y.Y. and S.Z.; Methodology, X.X.; Project administration, X.X.; Software, X.X.; Supervision, S.C.; Validation, Y.Y. and S.Z.; Writing—original draft, X.X.; Writing—review & editing, S.C. All authors have read and agreed to the published version of the manuscript.

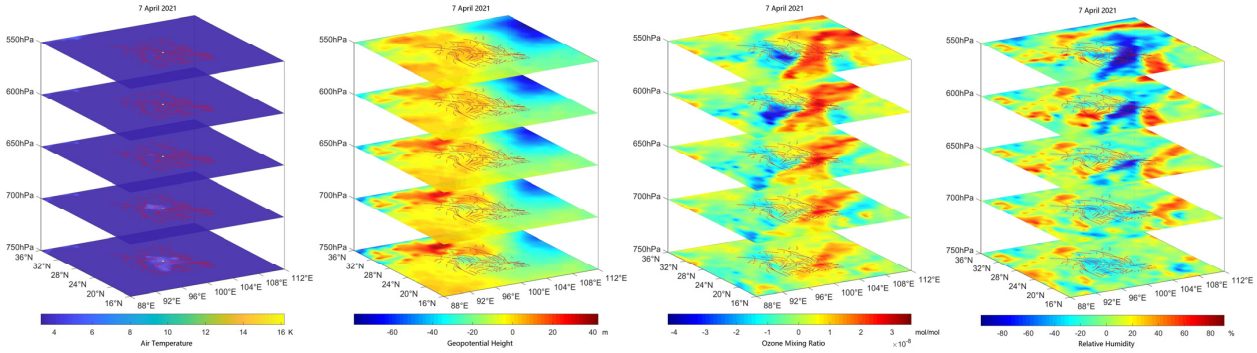
Funding: This research was funded by the National Key Research and Development Program of China (Grant No. 2020YFA0714103) and the program for JLU science and technology innovative research team (Grant No. JLUSTIRT, 2017TD-26).

Acknowledgments: The authors are thankful to National Center for Environmental Prediction of America for provision of the data used in this study. Furthermore, we thank the editors and reviewers for their constructive suggestions and insightful comments, which helped us greatly improve this manuscript.

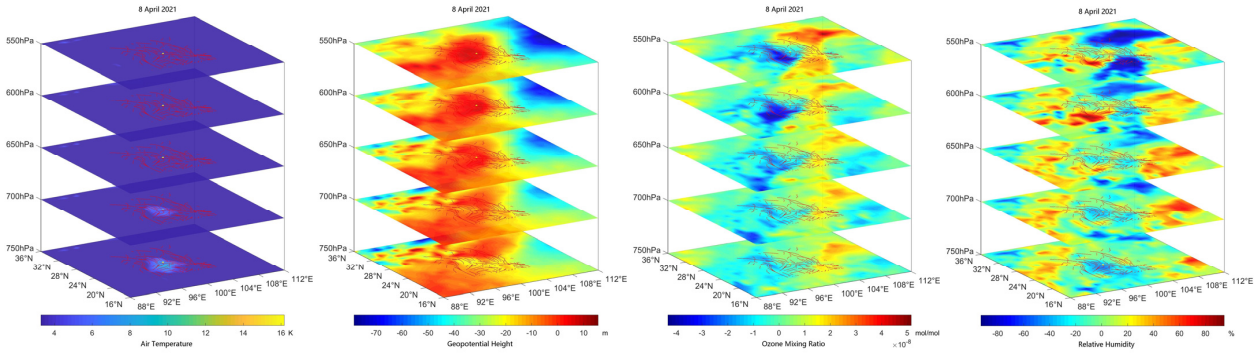
Conflicts of Interest: The authors declare no conflict of interest.

Appendix A

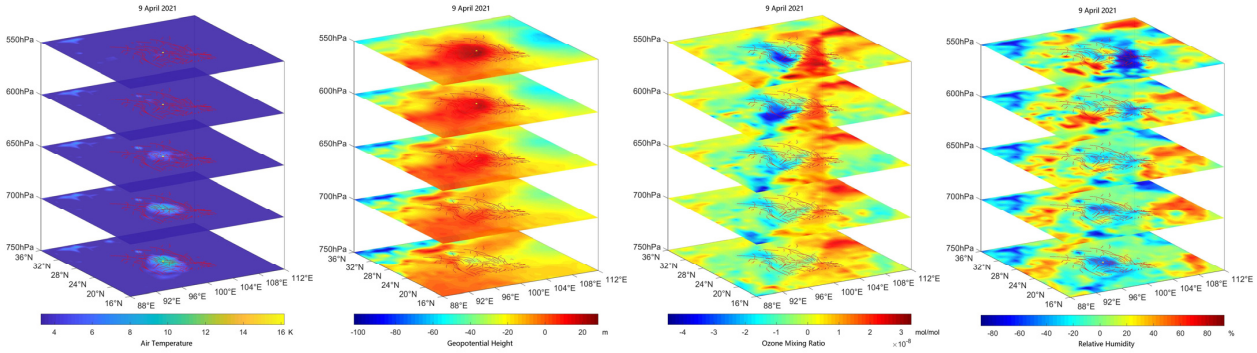
The evolution of atmospheric parameters during thermal anomalies associated with earthquakes in four seismogenic zones are shown in Figures A1–A4.



(**a**)

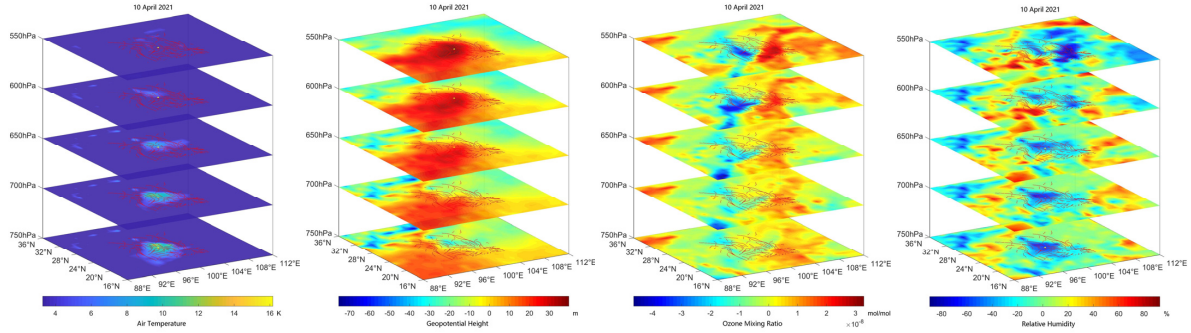


(**b**)

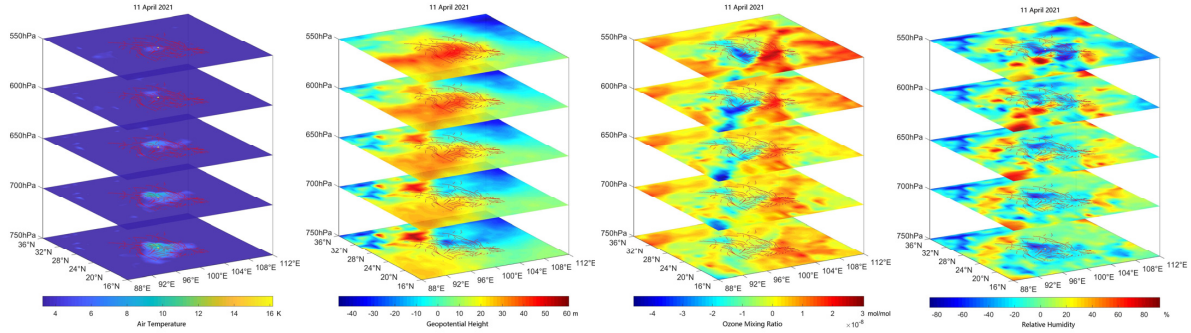


(**c**)

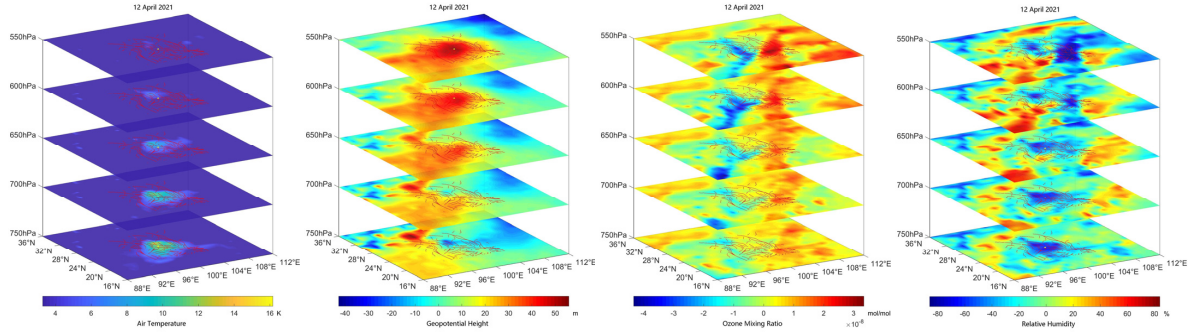
Figure A1. *Cont.*



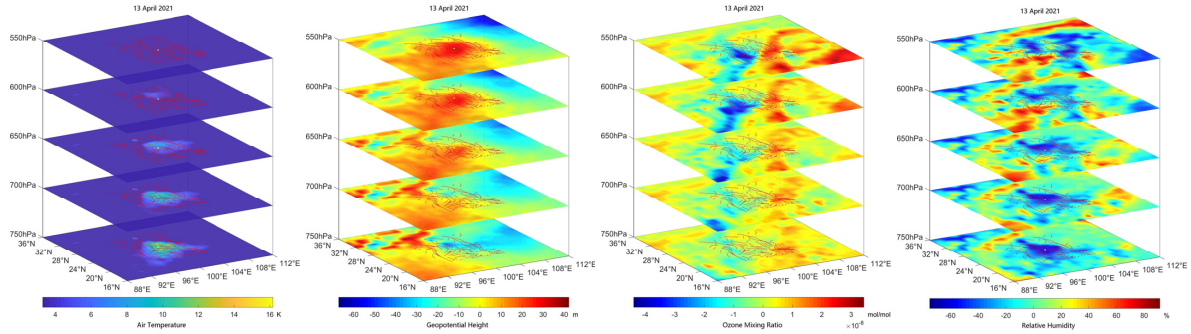
(**d**)



(**e**)

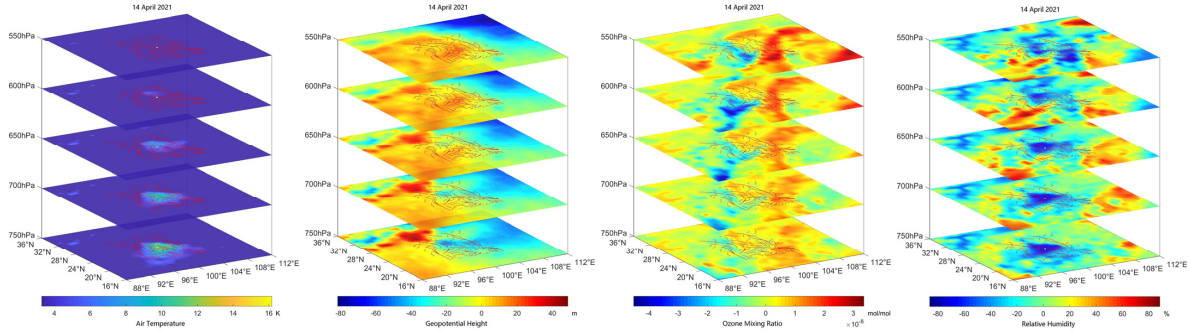


(**f**)

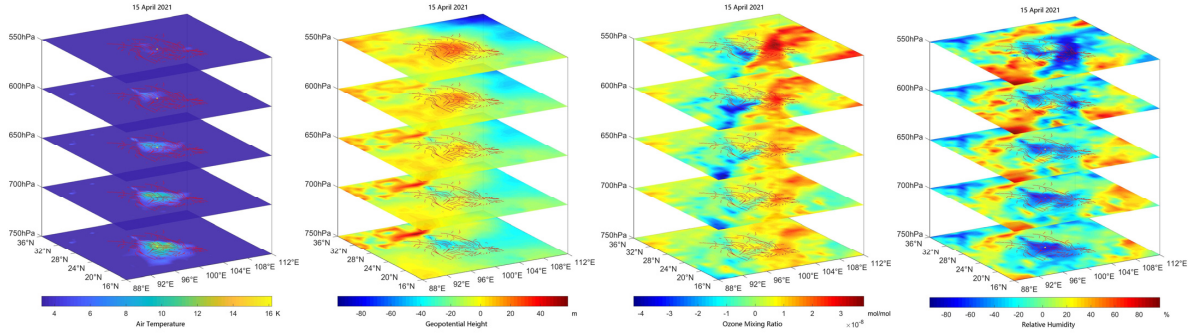


(**g**)

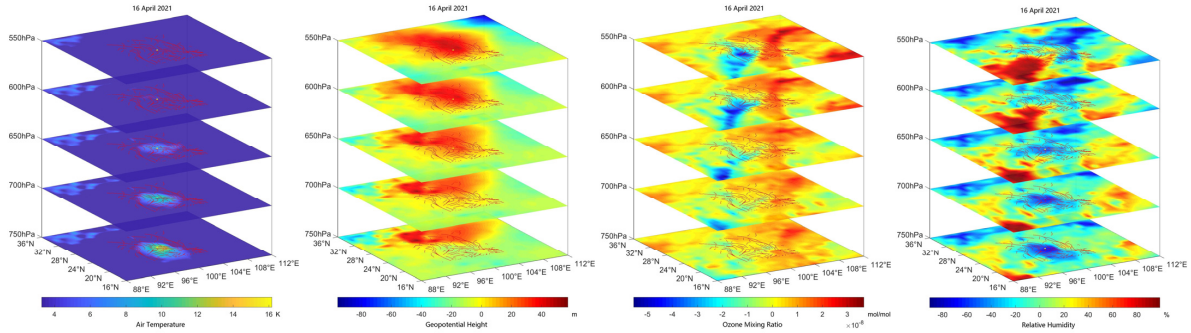
Figure A1. *Cont*.



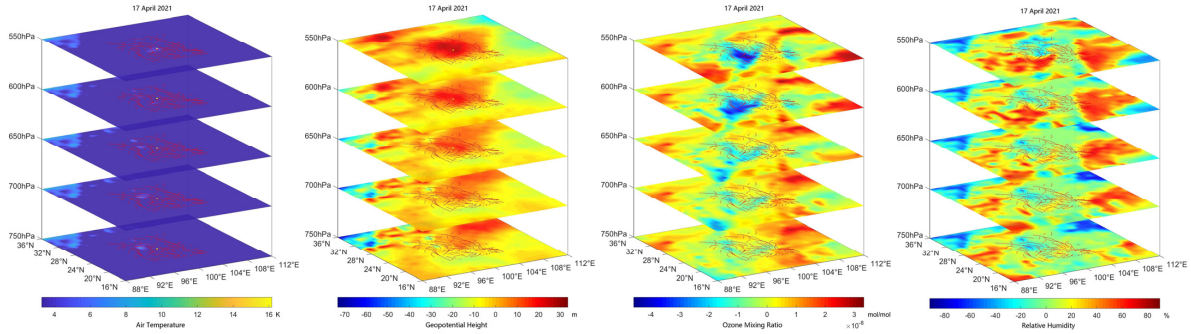
(**h**)



(**i**)

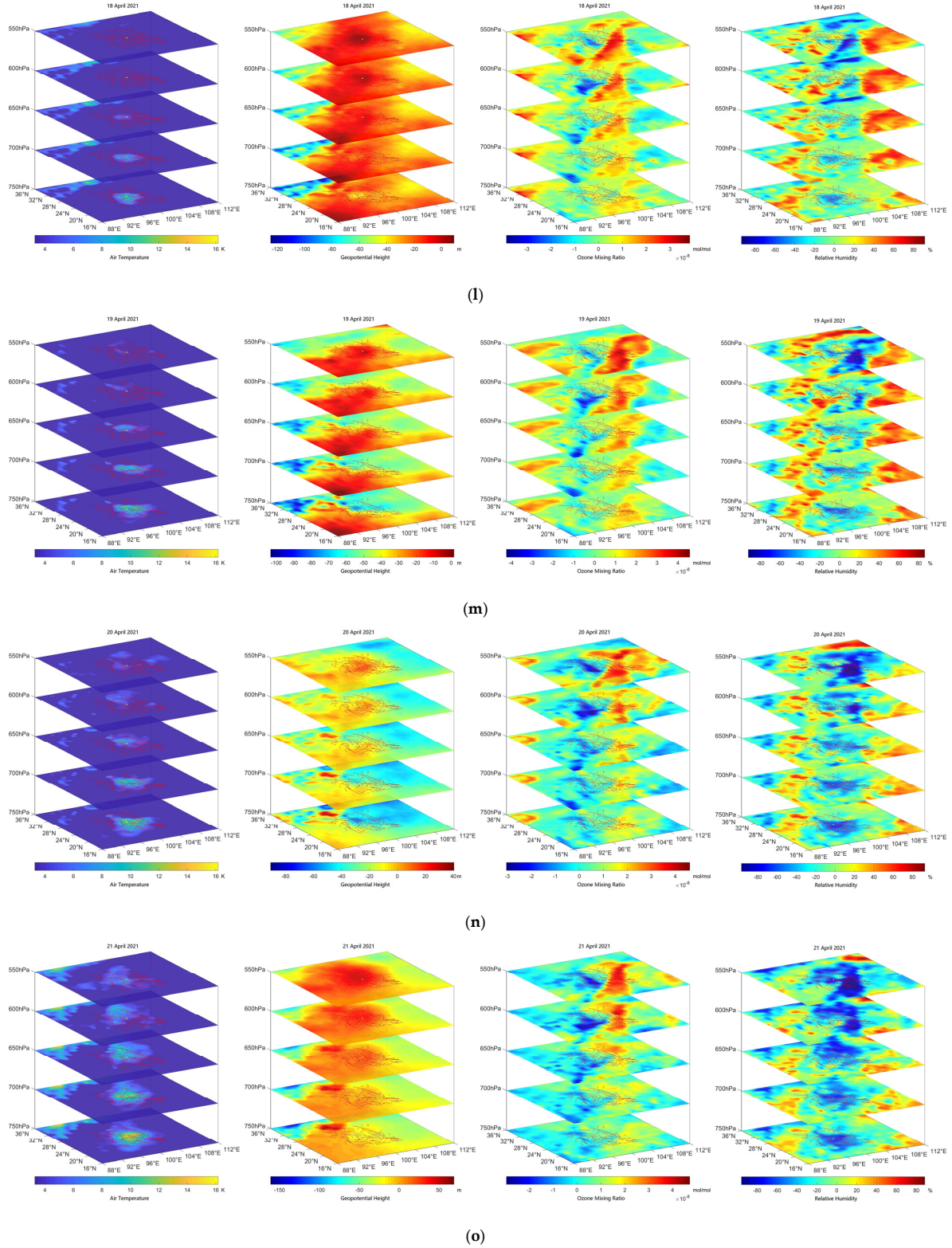


(**j**)



(**k**)

Figure A1. *Cont*.



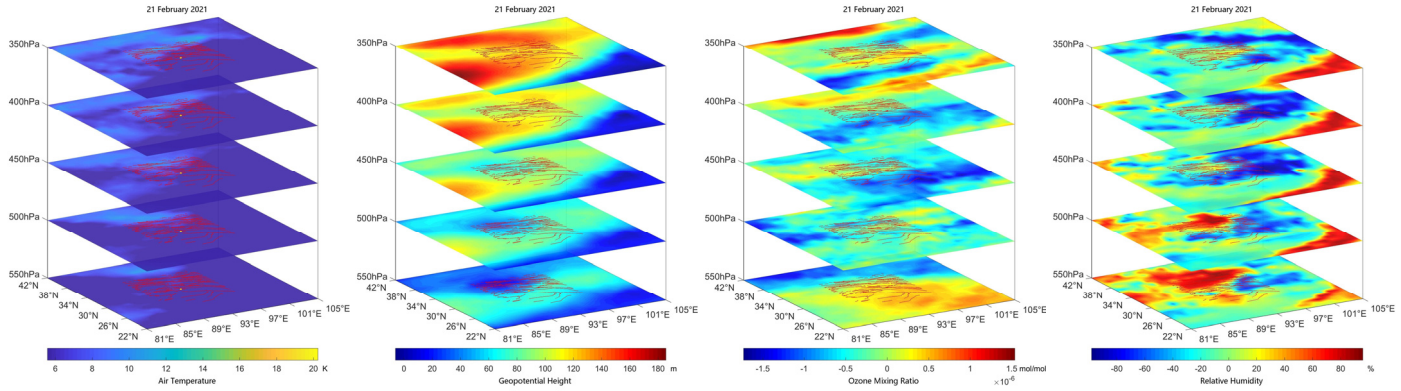
(**l**)

(**m**)

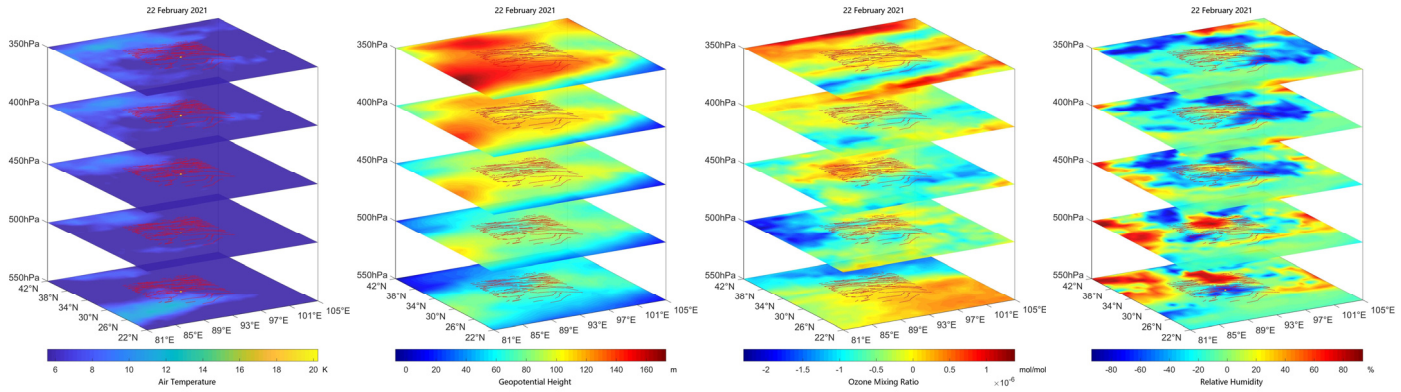
(**n**)

(**o**)

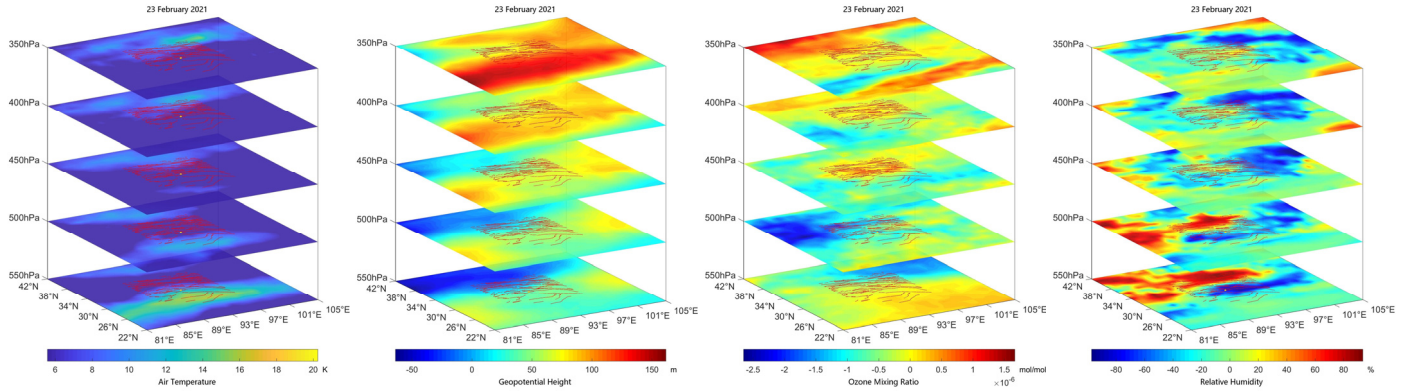
Figure A1. Composite atmospheric anomaly maps during atmospheric thermal anomalies associated with earthquake in Yangbi on (**a**) 7 April; (**b**) 8 April; (**c**) 9 April; (**d**) 10 April; (**e**) 11 April; (**f**) 12 April; (**g**) 13 April; (**h**) 14 April; (**i**) 15 April; (**j**) 16 April; (**k**) 17 April; (**l**) 18 April; (**m**) 19 April; (**n**) 20 April; (**o**) 21 April, 2021. The epicenter and faults are shown by yellow point and red lines, respectively. For each row, the subplots represent air temperature, geopotential height, ozone mixing ratio and relative humidity from left to right.



(**a**)

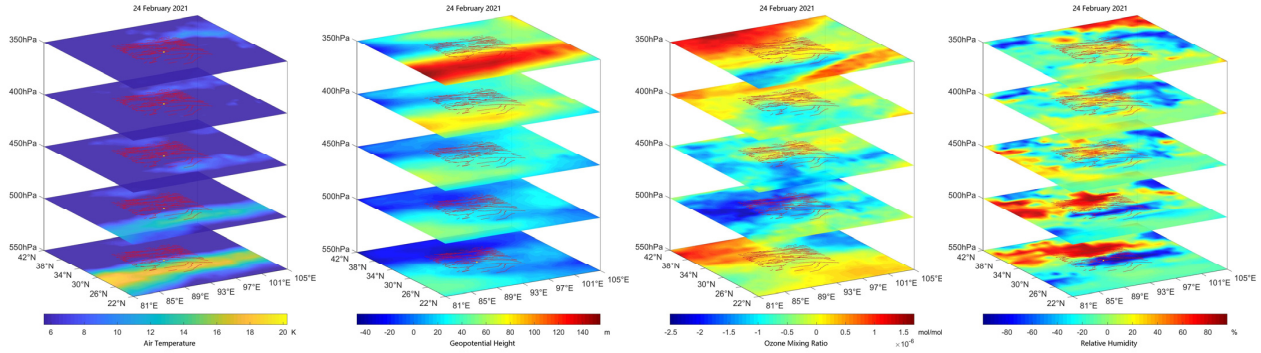


(**b**)

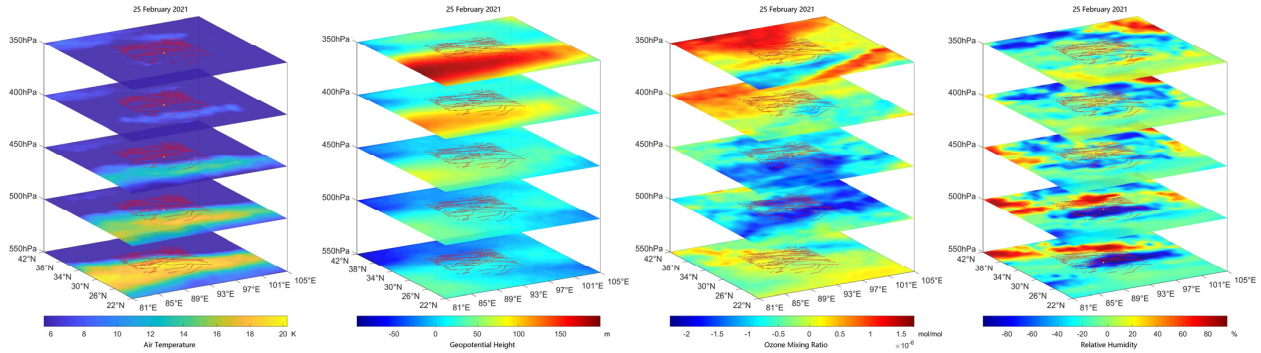


(**c**)

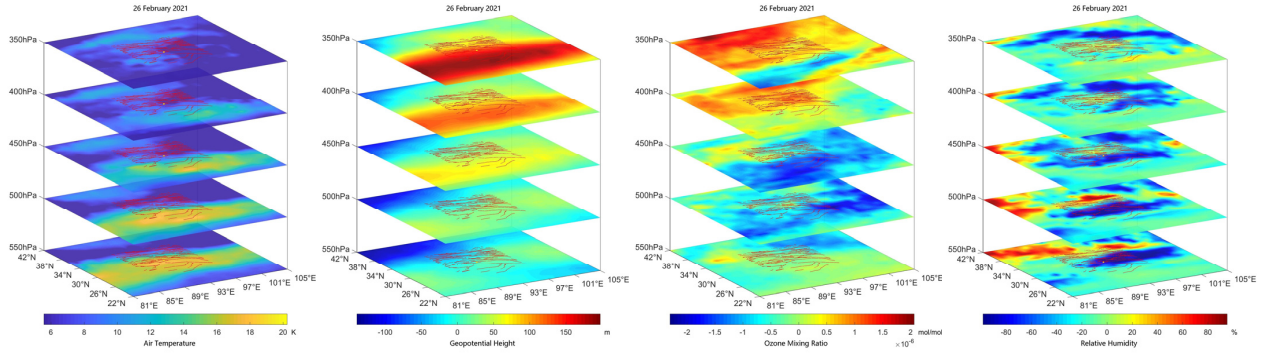
Figure A2. *Cont.*



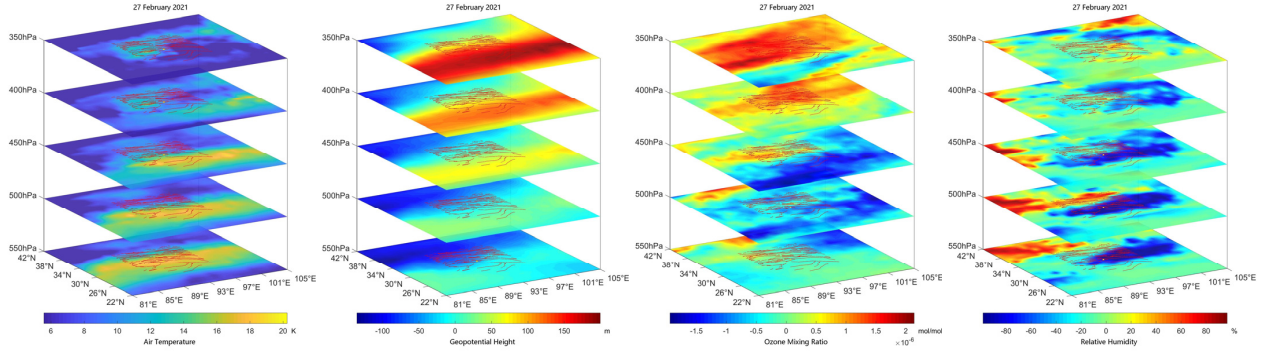
(**d**)



(**e**)

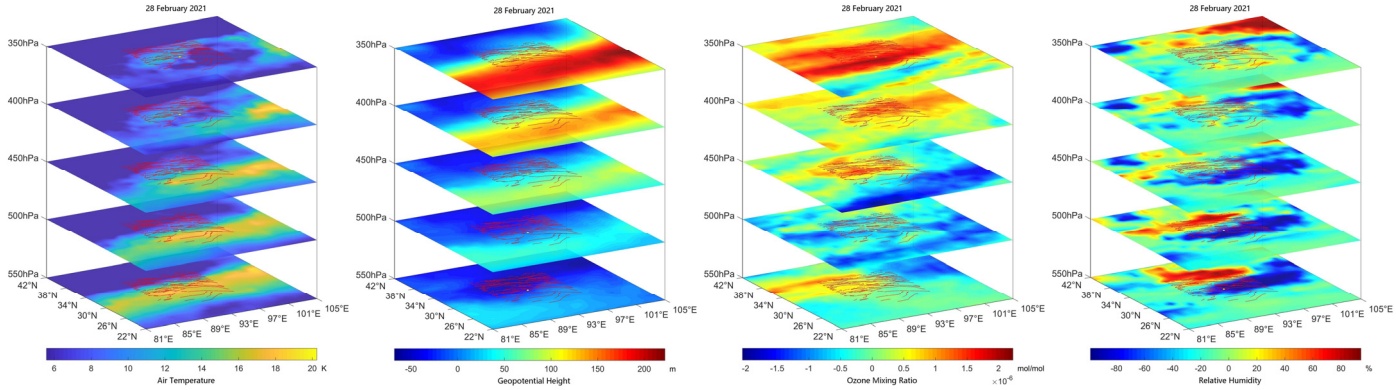


(**f**)



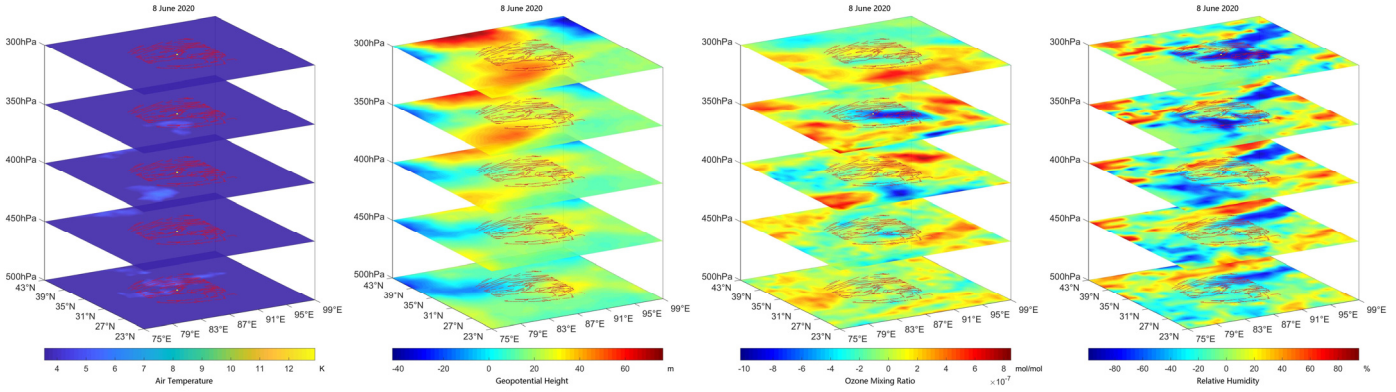
(**g**)

Figure A2. *Cont*.

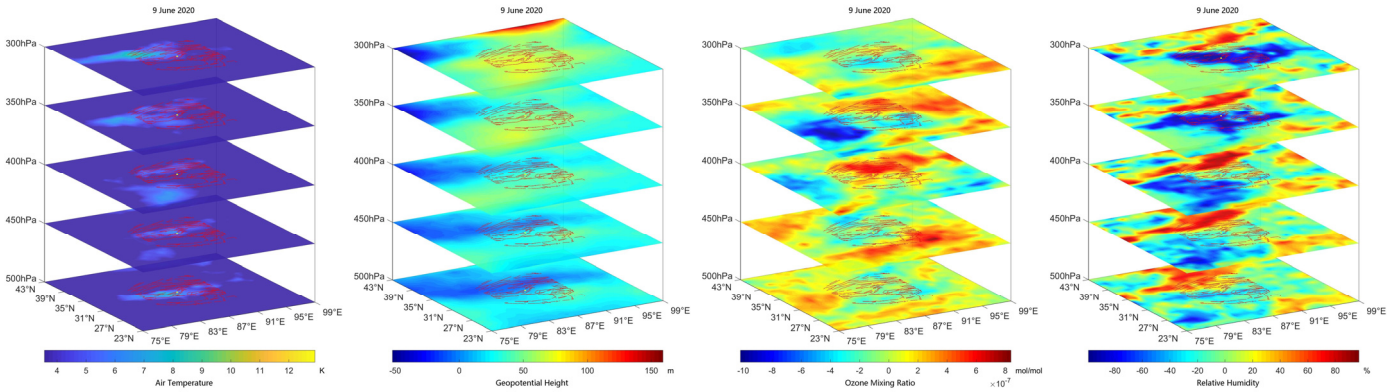


(**h**)

Figure A2. Composite atmospheric anomaly maps during atmospheric thermal anomalies associated with earthquake in Biru on (**a**) 21 February; (**b**) 22 February; (**c**) 23 February; (**d**) 24 February; (**e**) 25 February; (**f**) 26 February; (**g**) 27 February; (**h**) 28 February, 2021. The epicenter and faults are shown by yellow point and red lines, respectively. For each row, the subplots represent air temperature, geopotential height, ozone mixing ratio and relative humidity from left to right.

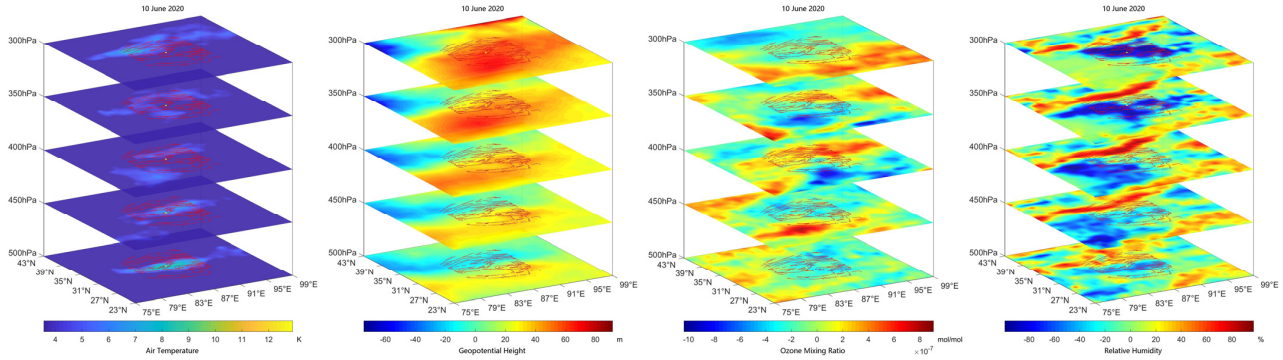


(**a**)

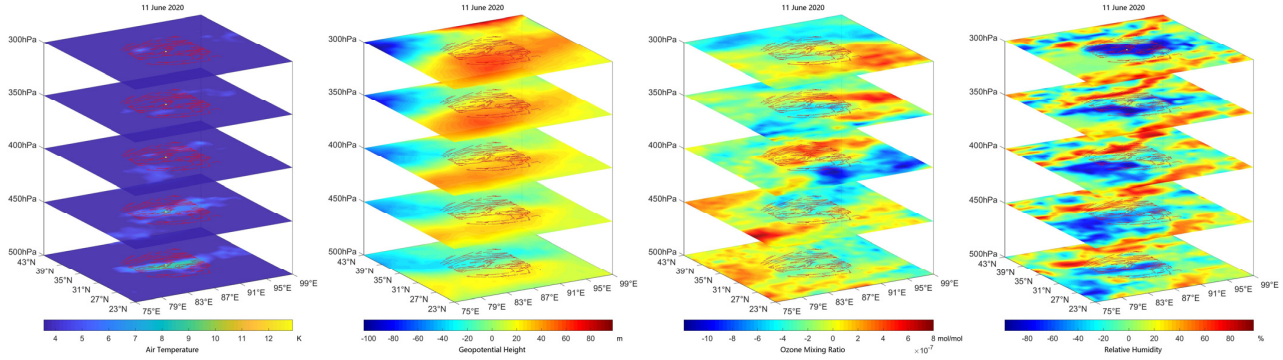


(**b**)

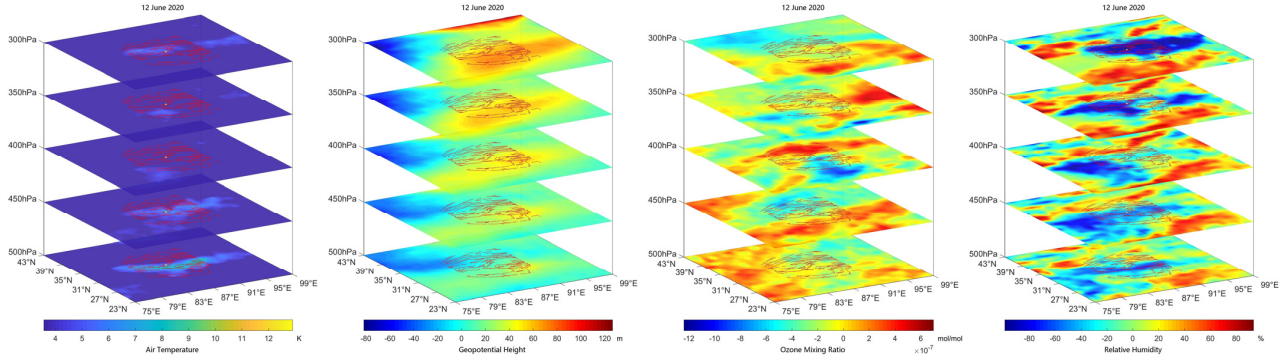
Figure A3. *Cont*.



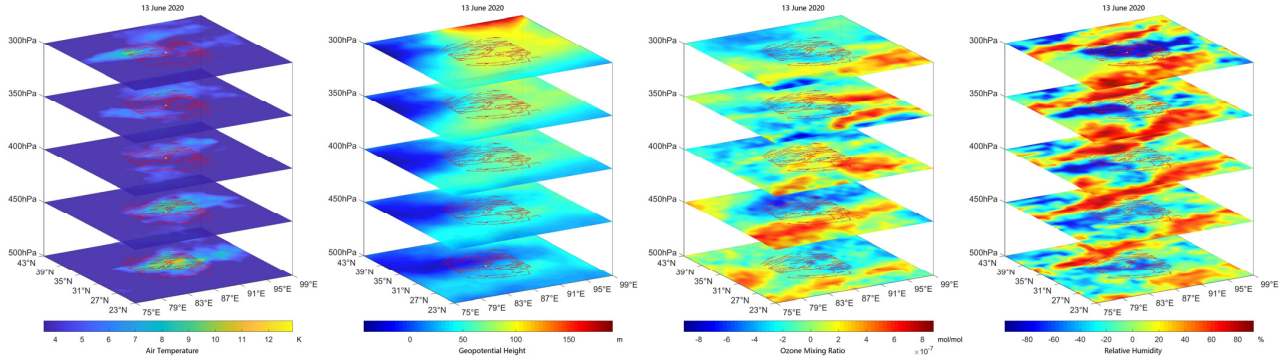
(**c**)



(**d**)

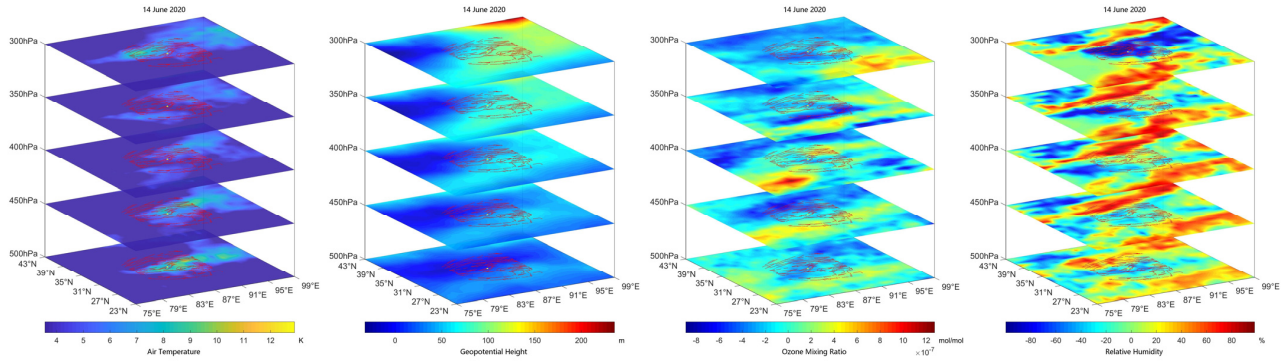


(**e**)

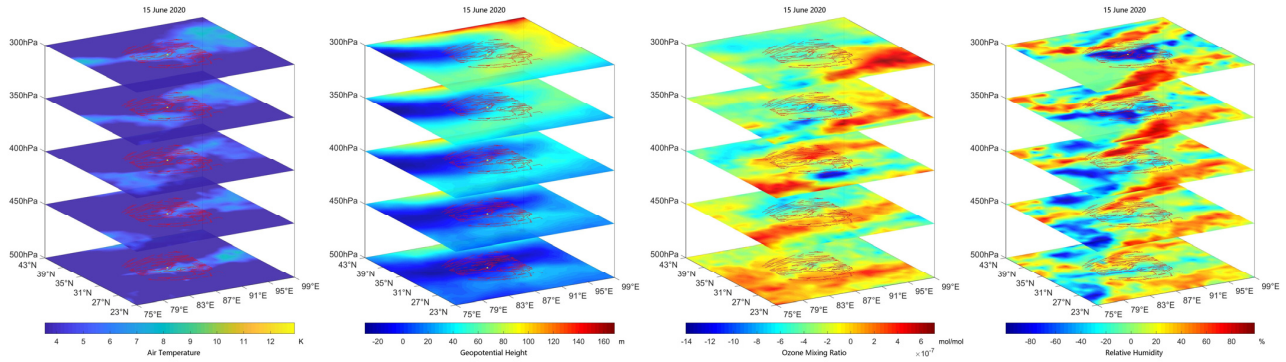


(**f**)

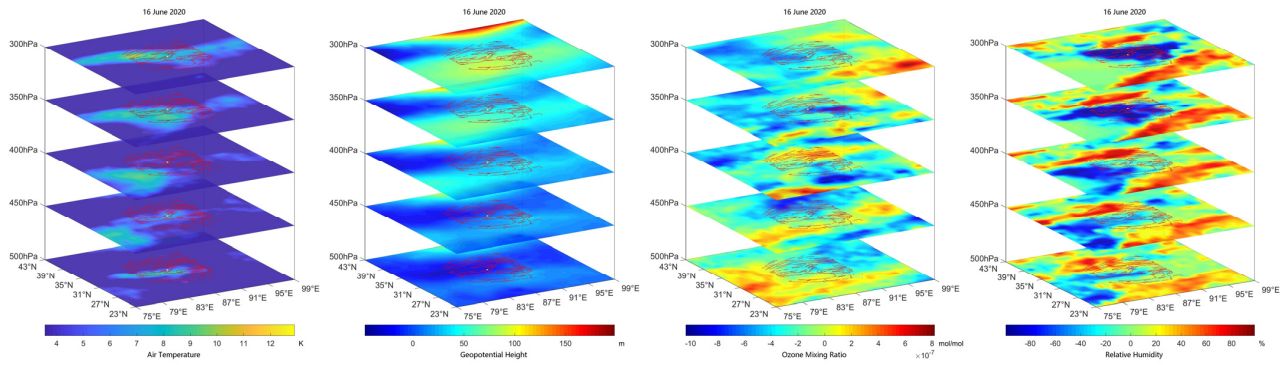
Figure A3. *Cont*.



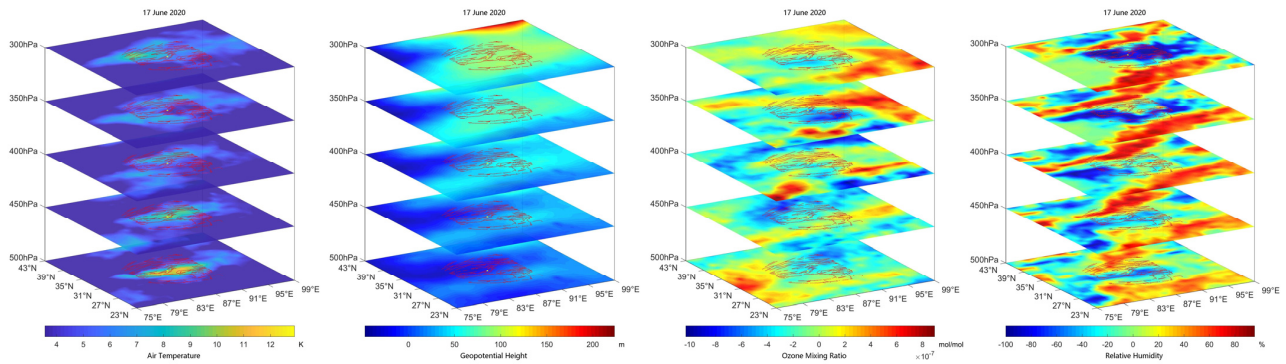
(**g**)



(**h**)

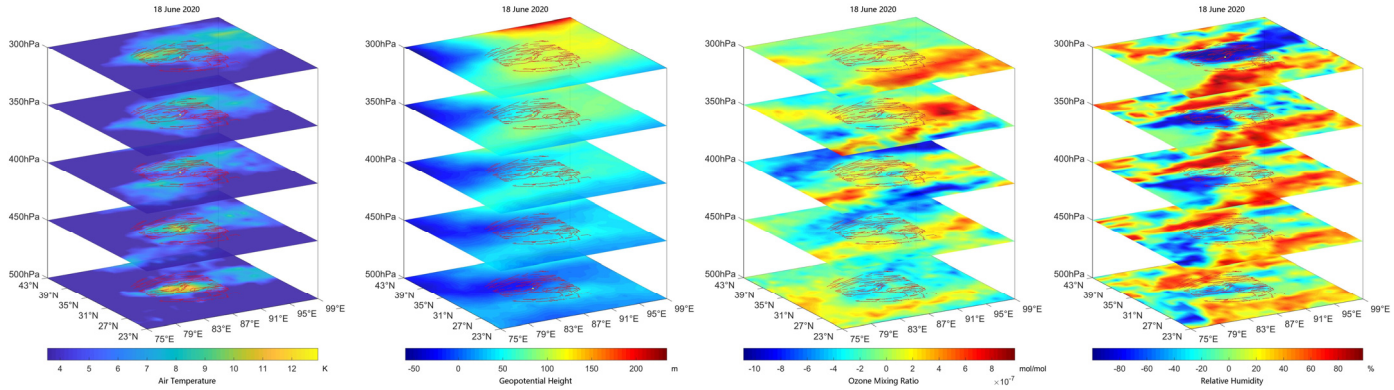


(**i**)

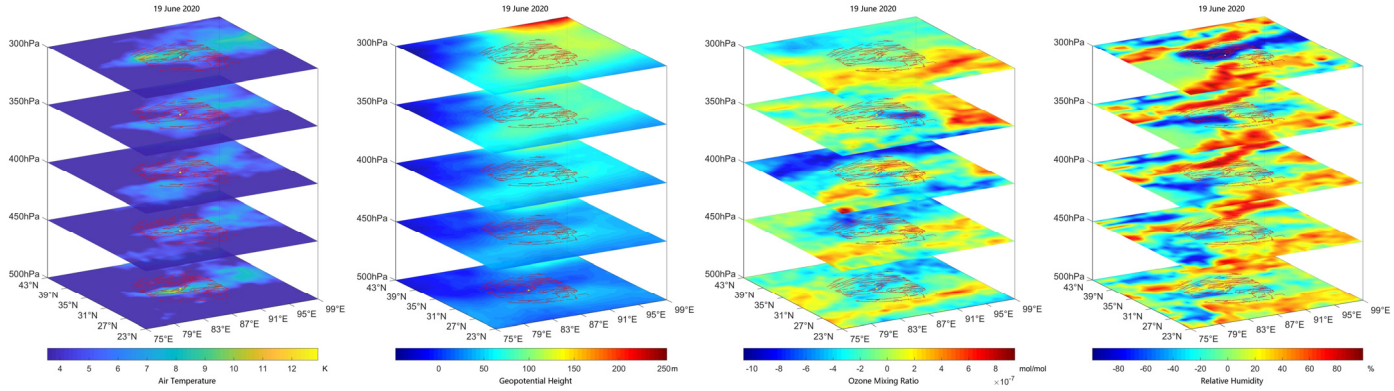


(**j**)

Figure A3. *Cont*.

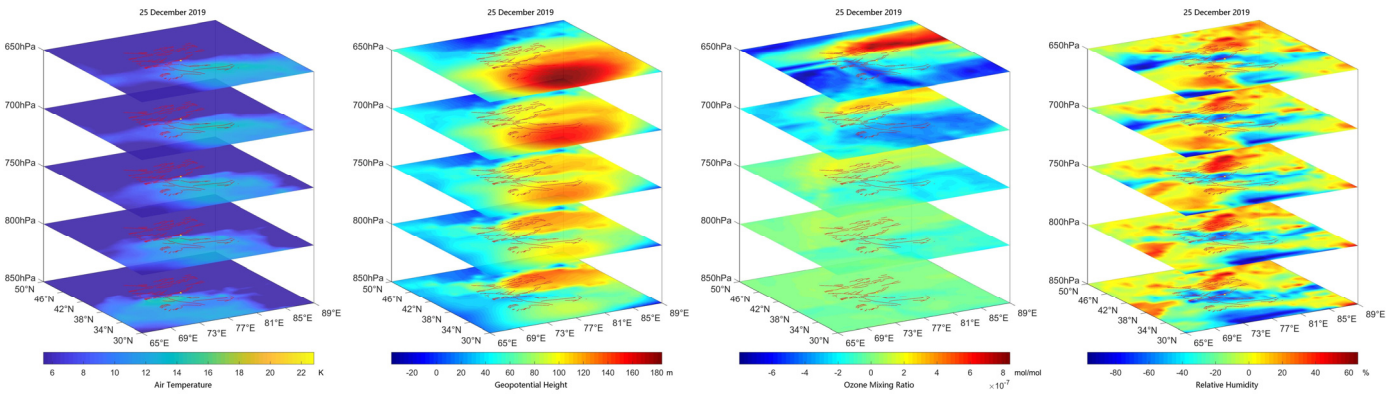


(**k**)



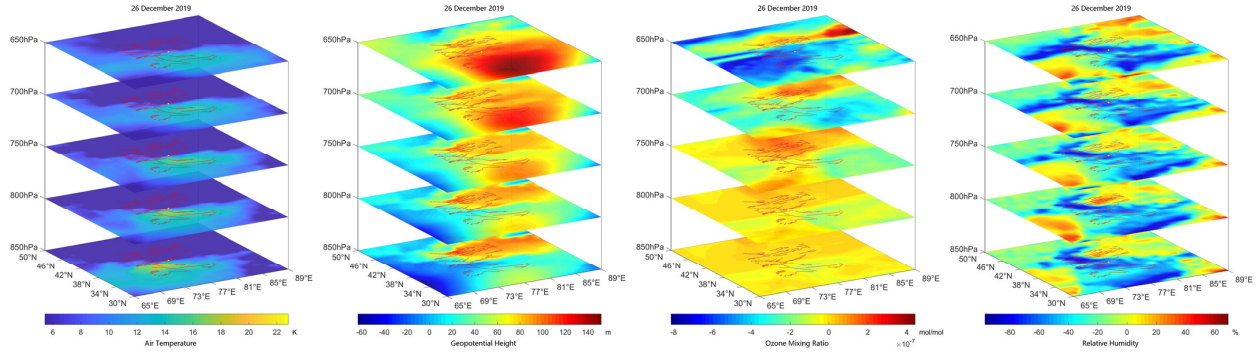
(**l**)

Figure A3. Composite atmospheric anomaly maps during atmospheric thermal anomalies associated with earthquake in Nima on (**a**) 8 June; (**b**) 9 June; (**c**) 10 June; (**d**) 11 June; (**e**) 12 June; (**f**) 13 June; (**g**) 14 June; (**h**) 15 June; (**i**) 16 June; (**j**) 17 June; (**k**) 18 June; (**l**) 19 June, 2020. The epicenter and faults are shown by yellow point and red lines, respectively. For each row, the subplots represent air temperature, geopotential height, ozone mixing ratio and relative humidity from left to right.

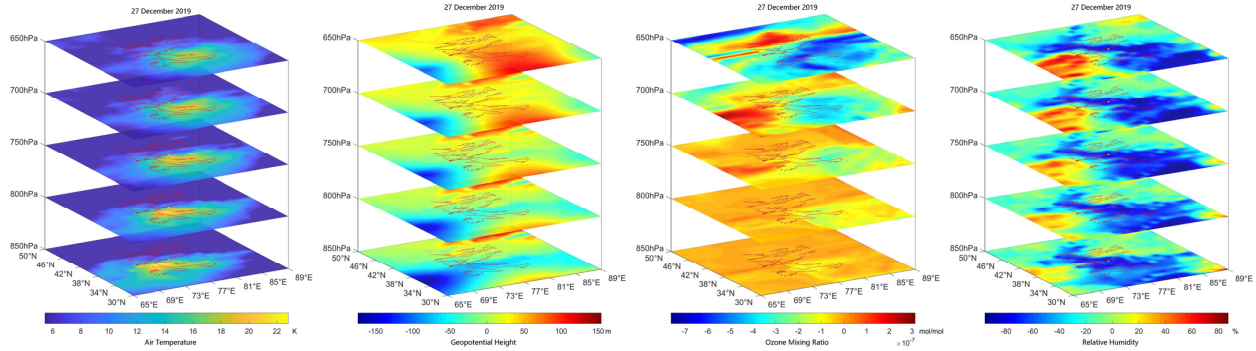


(**a**)

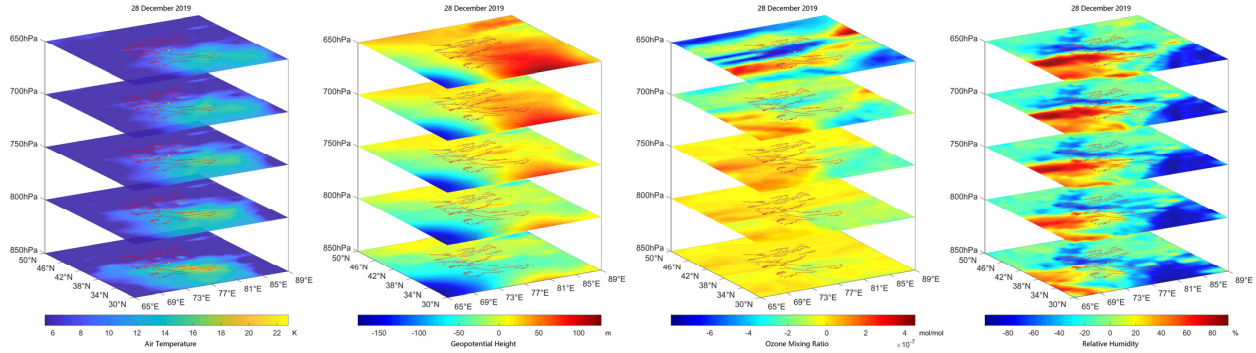
Figure A4. *Cont.*



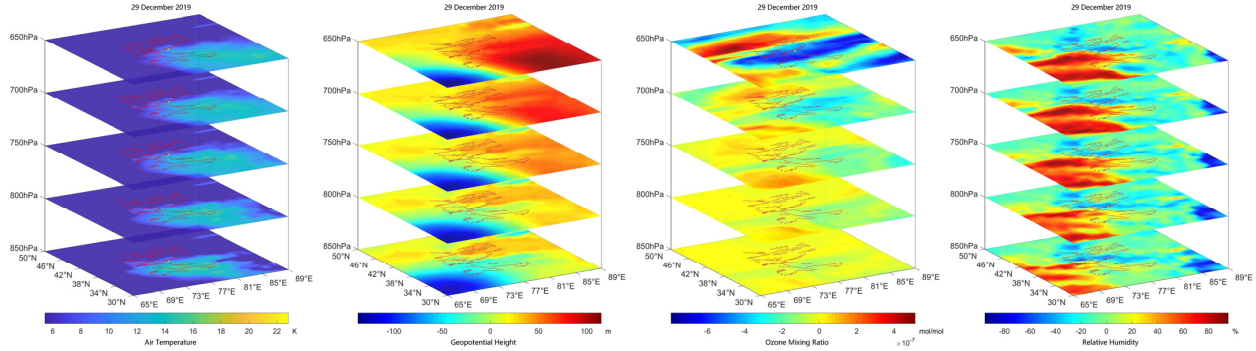
(**b**)



(**c**)



(**d**)



(**e**)

Figure A4. Composite atmospheric anomaly maps during atmospheric thermal anomalies associated with earthquake in Jiashi on (**a**) 25 December; (**b**) 26 December; (**c**) 27 December; (**d**) 28 December; (**e**) 29 December, 2019. The epicenter and faults are shown by yellow point and red lines, respectively. For each row, the subplots represent air temperature, geopotential height, ozone mixing ratio and relative humidity from left to right.

References

1. Singh, R.; Cervone, G.; Kafatos, M.; Prasad, A.; Sahoo, A.; Sun, D.; Tang, D.; Yang, R. Multi-sensor studies of the Sumatra earthquake and tsunami of 26 December 2004. *Int. J. Remote Sens.* **2007**, *28*, 2885–2896. [CrossRef]
2. Ouzounov, D.; Freund, F. Mid-infrared emission prior to strong earthquakes analyzed by remote sensing data. *Adv. Space Res.* **2004**, *33*, 268–273. [CrossRef]
3. Panda, S.; Choudhury, S.; Saraf, A.; Das, J. MODIS land surface temperature data detects thermal anomaly preceding 8 October 2005 Kashmir earthquake. *Int. J. Remote Sens.* **2007**, *28*, 4587–4596. [CrossRef]
4. Pulinets, S.; Ouzounov, D.; Ciraolo, L.; Singh, R.; Cervone, G.; Leyva, A.; Dunajecka, M.; Karelin, A.; Boyarchuk, K.; Kotsarenko, A. Thermal, atmospheric and ionospheric anomalies around the time of the Colima M7. 8 earthquake of 21 January 2003. *Ann. Geophys.* **2006**, *24*, 835–849. [CrossRef]
5. Jing, F.; Shen, X.; Kang, C.; Xiong, P. Variations of multi-parameter observations in atmosphere related to earthquake. *Nat. Hazards Earth Syst. Sci.* **2013**, *13*, 27–33. [CrossRef]
6. Wu, L.; Zheng, S.; De Santis, A.; Qin, K.; Mauro, R.D.; Liu, S.; Rainone, M.L. Geosphere coupling and hydrothermal anomalies before the 2009 M w 6.3 L'Aquila earthquake in Italy. *Nat. Hazards Earth Syst. Sci.* **2016**, *16*, 1859–1880. [CrossRef]
7. Lu, X.; Meng, Q.; Gu, X.; Zhang, X.; Xie, T.; Geng, F. Thermal infrared anomalies associated with multi-year earthquakes in the Tibet region based on China's FY-2E satellite data. *Adv. Space Res.* **2016**, *58*, 989–1001. [CrossRef]
8. Shah, M.; Tariq, M.A.; Naqvi, N.A. Atmospheric anomalies associated with Mw> 6.0 earthquakes in Pakistan and Iran during 2010–2017. *J. Atmos. Sol.-Terr. Phys.* **2019**, *191*, 105056. [CrossRef]
9. Jing, F.; Singh, R.P.; Shen, X. Land–atmosphere–meteorological coupling associated with the 2015 Gorkha (M 7.8) and Dolakha (M 7.3) Nepal earthquakes. *Geomat. Nat. Hazards Risk* **2019**, *10*, 1267–1284. [CrossRef]
10. Qi, Y.; Wu, L.; Mao, W.; Ding, Y.; He, M. Discriminating possible causes of microwave brightness temperature positive anomalies related with May 2008 Wenchuan earthquake sequence. *IEEE Trans. Geosci. Remote Sens.* **2020**, *59*, 1903–1916. [CrossRef]
11. Tramutoli, V.; Corrado, R.; Filizzola, C.; Genzano, N.; Lisi, M.; Pergola, N. From visual comparison to Robust Satellite Techniques: 30 years of thermal infrared satellite data analyses for the study of earthquake preparation phases. *Boll. Di Geofis. Teor. Ed Appl.* **2015**, *56*, 167–202.
12. Qiang, Z.; Dian, C.; Li, L.; Xu, M.; Ge, F.; Liu, T.; Zhao, Y.; Guo, M. Atellitic thermal infrared brightness temperature anomaly image—short-term and impending earthquake precursors. *Sci. China Ser. D: Earth Sci.* **1999**, *42*, 313–324. [CrossRef]
13. Tronin, A.A.; Hayakawa, M.; Molchanov, O.A. Thermal IR satellite data application for earthquake research in Japan and China. *J. Geodyn.* **2002**, *33*, 519–534. [CrossRef]
14. Tramutoli, V. Robust Satellite Techniques (RST) for natural and environmental hazards monitoring and mitigation: Ten years of successful applications. In Proceedings of the ISPMSRS 2005 Conference, Beijing, China, 17–19 October 2005.
15. Tramutoli, V. Robust satellite techniques (RST) for natural and environmental hazards monitoring and mitigation: Theory and applications. In Proceedings of the 2007 International Workshop on the Analysis of Multi-temporal Remote Sensing Images, Leuven, Belgium, 18–20 July 2007; pp. 1–6.
16. Zhang, Y.; Guo, X.; Zhong, M.; Shen, W.; Li, W.; He, B. Wenchuan earthquake: Brightness temperature changes from satellite infrared information. *Chin. Sci. Bull.* **2010**, *55*, 1917–1924. [CrossRef]
17. Chen, S.; Liu, P.; Feng, T.; Wang, D.; Jiao, Z.; Chen, L.; Xu, Z.; Zhang, G. Exploring Changes in Land Surface Temperature Possibly Associated with Earthquake: Case of the April 2015 Nepal Mw 7.9 Earthquake. *Entropy* **2020**, *22*, 377. [CrossRef]
18. Blackett, M.; Wooster, M.J.; Malamud, B.D. Exploring land surface temperature earthquake precursors: A focus on the Gujarat (India) earthquake of 2001. *Geophys. Res. Lett.* **2011**, *38*. [CrossRef]
19. Guangmeng, G.; Bin, W. Cloud anomaly before Iran earthquake. *Int. J. Remote Sens.* **2008**, *29*, 1921–1928.
20. Guangmeng, G.; Jie, Y. Three attempts of earthquake prediction with satellite cloud images. *Nat. Hazards Earth Syst. Sci.* **2013**, *13*, 91–95. [CrossRef]
21. Zhang, Y.; Meng, Q. A statistical analysis of TIR anomalies extracted by RSTs in relation to an earthquake in the Sichuan area using MODIS LST data. *Nat. Hazards Earth Syst. Sci.* **2019**, *19*, 535–549. [CrossRef]
22. Kilston, S.; Knopoff, L. Lunar–solar periodicities of large earthquakes in southern California. *Nature* **1983**, *304*, 21–25. [CrossRef]
23. Zhang, X.; Kang, C.; Ma, W.; Ren, J.; Wang, Y. Study on thermal anomalies of earthquake process by using tidal-force and outgoing-longwave-radiation. *Therm. Sci.* **2018**, *22*, 767–776. [CrossRef]
24. Heaton, T.H. Tidal triggering of earthquakes. *Geophys. J. Int.* **1975**, *43*, 307–326. [CrossRef]
25. Zhang, Y.; Meng, Q.; Wang, Z.; Lu, X.; Hu, D. Temperature Variations in Multiple Air Layers before the Mw 6.2 2014 Ludian Earthquake, Yunnan, China. *Remote Sens.* **2021**, *13*, 884. [CrossRef]
26. Ma, W.; Zhang, X.; Liu, J.; Yao, Q.; Zhou, B.; Yue, C.; Kang, C.; Lu, X. Influences of multiple layers of air temperature differences on tidal forces and tectonic stress before, during and after the Jiujiang earthquake. *Remote Sens. Environ.* **2018**, *210*, 159–165.
27. Cui, Y.; Ouzounov, D.; Hatzopoulos, N.; Sun, K.; Zou, Z.; Du, J. Satellite observation of CH4 and CO anomalies associated with the Wenchuan MS 8.0 and Lushan MS 7.0 earthquakes in China. *Chem. Geol.* **2017**, *469*, 185–191. [CrossRef]
28. Cui, J.; Shen, X.; Zhang, J.; Ma, W.; Chu, W. Analysis of spatiotemporal variations in middle-tropospheric to upper-tropospheric methane during the Wenchuan M s = 8.0 earthquake by three indices. *Nat. Hazards Earth Syst. Sci.* **2019**, *19*, 2841–2854. [CrossRef]

29. Liu, Q.; De Santis, A.; Piscini, A.; Cianchini, G.; Ventura, G.; Shen, X. Multi-parametric climatological analysis reveals the involvement of fluids in the preparation phase of the 2008 Ms 8.0 wenchuan and 2013 Ms 7.0 lushan earthquakes. *Remote Sens.* **2020**, *12*, 1663. [CrossRef]
30. Dunajecka, M.; Pulinets, S. Atmospheric and thermal anomalies observed around the time of strong earthquakes in Mexico. *Atmósfera* **2005**, *18*, 235–247.
31. Shah, M.; Aibar, A.C.; Tariq, M.A.; Ahmed, J.; Ahmed, A. Possible ionosphere and atmosphere precursory analysis related to Mw> 6.0 earthquakes in Japan. *Remote Sens. Environ.* **2020**, *239*, 111620. [CrossRef]
32. Pulinets, S.; Ouzounov, D. Lithosphere—Atmosphere—Ionosphere Coupling (LAIC) model—An unified concept for earthquake precursors validation. *J. Asian Earth Sci.* **2011**, *41*, 371–382. [CrossRef]
33. Akhoondzadeh, M.; De Santis, A.; Marchetti, D.; Piscini, A.; Cianchini, G. Multi precursors analysis associated with the powerful Ecuador (M W =7.8) earthquake of 16 April 2016 using Swarm satellites data in conjunction with other multi-platform satellite and ground data. *Adv. Space Res.* **2018**, *61*, 248–263. [CrossRef]
34. Qin, K.; Wu, L.; Santis, A.D.; Meng, J.; Ma, W.; Cianchini, G. Quasi-synchronous multi-parameter anomalies associated with the 2010–2011 New Zealand earthquake sequence. *Nat. Hazards Earth Syst. Sci.* **2012**, *12*, 1059–1072. [CrossRef]
35. Genzano, N.; Filizzola, C.; Hattori, K.; Pergola, N.; Tramutoli, V. Statistical Correlation Analysis Between Thermal Infrared Anomalies Observed from MTSATs and Large Earthquakes Occurred in Japan (2005–2015). *J. Geophys. Res. Solid Earth* **2021**, *126*, e2020JB020108. [CrossRef]
36. Kalnay, E.; Kanamitsu, M.; Kistler, R.; Collins, W.; Deaven, D.; Gandin, L.; Iredell, M.; Saha, S.; White, G.; Woollen, J. The NCEP/NCAR 40-year reanalysis project. *Bull. Am. Meteorol. Soc.* **1996**, *77*, 437–472. [CrossRef]
37. Kistler, R.; Kalnay, E.; Collins, W.; Saha, S.; White, G.; Woollen, J.; Chelliah, M.; Ebisuzaki, W.; Kanamitsu, M.; Kousky, V. The NCEP/NCAR 50-year reanalysis: Documentation and monthly-means CD-ROM. *Bull. Am. Meteorol. Soc.* **2001**, *82*. [CrossRef]
38. Straser, V. Variations in gravitational field, tidal force, electromagnetic waves and earthquakes. *New Concepts Glob. Tecton. Newsl.* **2010**, *57*, 98–108.
39. Ma, W.; Wang, H.; Li, F.; Ma, W. Relation between the celestial tide-generating stress and the temperature variations of the Abruzzo M= 6.3 Earthquake in April 2009. *Nat. Hazards Earth Syst. Sci.* **2012**, *12*, 819–827. [CrossRef]
40. Zhou, S.; Zhang, R. Decadal variations of temperature and geopotential height over the Tibetan Plateau and their relations with Tibet ozone depletion. *Geophys. Res. Lett.* **2005**, *32*, 32. [CrossRef]
41. Tomczyk, A.M.; Bednorz, E. Heat waves in Central Europe and tropospheric anomalies of temperature and geopotential heights. *Int. J. Climatol.* **2019**, *39*, 4189–4205. [CrossRef]
42. Zheng, S.; Singh, R.P. Aerosol and meteorological parameters associated with the intense dust event of 15 April 2015 over Beijing, China. *Remote Sens.* **2018**, *10*, 957. [CrossRef]
43. Jing, F.; Chauhan, A.; P. Singh, R.; Dash, P. Changes in atmospheric, meteorological, and ocean parameters associated with the 12 January 2020 Taal volcanic eruption. *Remote Sens.* **2020**, *12*, 1026. [CrossRef]
44. Piscini, A.; De Santis, A.; Marchetti, D.; Cianchini, G. A Multi-parametric climatological approach to study the 2016 Amatrice–Norcia (Central Italy) earthquake preparatory phase. *Pure Appl. Geophys.* **2017**, *174*, 3673–3688. [CrossRef]
45. Xiong, P.; Tong, L.; Zhang, K.; Shen, X.; Battiston, R.; Ouzounov, D.; Iuppa, R.; Crookes, D.; Long, C.; Zhou, H. Towards advancing the earthquake forecasting by machine learning of satellite data. *Sci. Total. Environ.* **2021**, *771*, 145256. [CrossRef]
46. Jing, F.; Singh, R.P. Changes in Tropospheric Ozone Associated with Strong Earthquakes and Possible Mechanism. *IEEE J. Sel. Top. Appl. Earth Obs. Remote Sens.* **2021**, *14*, 5300–5310. [CrossRef]
47. Ouzounov, D.; Pulinets, S.; Liu, J.Y.; Hattori, K.; Han, P. Multiparameter Assessment of Pre-Earthquake Atmospheric Signals. In *Pre-Earthquake Processes: A Multidisciplinary Approach to Earthquake Prediction Studies*; AGU/Wiley: Hoboken, NJ, USA, 2018; pp. 339–359.
48. Meng, Q.; Zhang, Y. Discovery of spatial-temporal causal interactions between thermal and methane anomalies associated with the Wenchuan earthquake. *Eur. Phys. J. Spec. Top.* **2021**, *230*, 247–261. [CrossRef]
49. Varotsos, C.A.; Efstathiou, M.N.; Cracknell, A.P. On the association of aerosol optical depth and total ozone fluctuations with recent earthquakes in Greece. *Acta Geophys.* **2017**, *65*, 659–665. [CrossRef]